Supplementary Information for

Optically Addressed Metasurface Spatial Light Modulator

Xuhao Fan[1], Wei Xiong[1,3], Ke Xu[1], Zhou Zhou[2], Xinger Wang[1], Zhilin Teng[1], Zongjing Li[1], Zexu Zhang[1], Xuan Yu[1], Zhongtian Nie[1], Jinsong Xia[1,3], Cheng-Wei Qiu[2]*, Hui Gao[1,3]**

[1] Wuhan National Laboratory for Optoelectronics and School of Optical and Electronic Information, Huazhong University of Science and Technology, Wuhan 430074, China.
[2] Department of Electrical and Computer Engineering, National University of Singapore, Singapore 117576, Singapore.
[3] Optics Valley Laboratory, Wuhan 430074, China.

**Corresponding author. E-mail: weixiong@hust.edu.cn (W. X.); chengwei.qiu@nus.edu.sg (C.-W. Q.); gaohui_wnlo@hust.edu.cn (H. G.).*

This document includes the following sections:

Other Supplementary Material for this manuscript includes the following:

Supplementary Movies S1 to S9

Supplementary Notes

Supplementary Note S1. Theoretical framework of optically addressed OA-MSLM.

Huygens' principle asserts that each point on a wavefront can be treated as the source of secondary wavelets that propagate outward, thereby reconstructing the entire wavefront. This principle has been widely utilized in metasurface design[1,2], where each meta-atom functions as a localized secondary source modulating the incident light's phase and amplitude. These individual meta-atoms collectively form a globally modulated light field, analogous to the reconstruction of a wavefront through secondary wavelets. In the context of an OA-MSLM, we treat a meta-atom supercell as an ensemble of secondary wavelet sources, consistent with the conceptual framework of Huygens' principle. When an addressing light beam interacts with the discrete meta-atom supercell, each addressed meta-atom imparts a local geometric phase shift determined by its rotational orientation and structural properties. Collectively, these localized modulations across the meta-atom supercell contribute to the overall modulation of the transmitted wavefront. As the addressing light beam varies, the resulting wavefront dynamically adjusts, enabling the desired modulation. Guided by this principle, we establish the theoretical framework and characterize the electromagnetic response of the optically addressed OA-MSLM.

1. Geometric phase of a single rectangular meta-atom

We first consider a single rectangular meta-atom, in which two orthogonal eigen-dipoles are excited along the short and long axes. The global coordinate system of the pre-discretized metasurface (PDM) is defined as the *x*–*y* coordinate system, while the local coordinate system of the anisotropic unit is defined as the *u*–*v* coordinate system. The angle θ between the global principal axis *x* and the local principal axis *u* represents the in-plane rotation of the anisotropic structure, as illustrated in Supplementary Fig. S1.

The rectangular meta-atom modulates the geometric phase of the incident polarized light by introducing a phase shift proportional to its in-plane rotation angle. The transmission of the electromagnetic wave through the meta-atom can be described using the Jones matrix formalism, which relates the input and output electric field components[3]. Accordingly, the output electric field distribution after passing through the anisotropic metasurface is expressed as:

$$\begin{bmatrix} E_{x\_out} \\ E_{y\_out} \end{bmatrix} = J_\theta \begin{bmatrix} E_{x\_in} \\ E_{y\_in} \end{bmatrix} \tag{S1}$$

Here, E_{x_in} and E_{y_in} denote the polarization components of the incident electromagnetic wave along the *x*- and *y*-axes, respectively. Likewise, E_{x_out} and E_{y_out} correspond to the polarization components of the transmitted electromagnetic wave along the same axes. The matrix J_θ represents the Jones matrix of the anisotropic metasurface, characterizing the modulation of the wave and describing the transformation of its polarization state upon interaction. For transmissive geometric phase metasurfaces, when the complex-amplitude transmission coefficients of the incident electromagnetic wave along the principal axes u

and v of the local coordinate system are denoted by t_u and t_v, respectively, the Jones matrix of the anisotropic unit in the local coordinate system can be written as:

$$J_\theta = \begin{bmatrix} t_u & 0 \\ 0 & t_v \end{bmatrix} \tag{S2}$$

A rotation matrix $R(\theta)$, which is related to the rotation angle of the anisotropic meta-atom, is defined as:

$$R(\theta) = \begin{pmatrix} \cos\theta & -\sin\theta \\ \sin\theta & \cos\theta \end{pmatrix} \tag{S3}$$

Using the above rotation matrix, the Jones matrix of the phase gradient metasurface in the global $x-y$ coordinate system can be derived as:

$$J = R(\theta)J_\theta R(-\theta) = \begin{bmatrix} t_u\cos^2\theta + t_v\sin^2\theta & (t_u - t_v)\sin\theta\cos\theta \\ (t_u - t_v)\sin\theta\cos\theta & t_u\sin^2\theta + t_v\cos^2\theta \end{bmatrix} \tag{S4}$$

When a circularly polarized electromagnetic wave is incident on the metasurface and modulated by its structure, the output electric field can be expressed as:

$$\begin{bmatrix} E_{x\_out} \\ E_{y\_out} \end{bmatrix} = \frac{J_\theta}{\sqrt{2}}\begin{bmatrix} 1 \\ i\sigma \end{bmatrix} = \frac{1}{2\sqrt{2}}\left((t_u + t_v)\begin{bmatrix} 1 \\ i\sigma \end{bmatrix} + (t_u - t_v)e^{2i\sigma\theta}\begin{bmatrix} 1 \\ -i\sigma \end{bmatrix}\right) \tag{S5}$$

where $\sigma = \pm 1$ corresponds to right circular polarization (RCP) and left circular polarization (LCP), respectively. When an LCP or RCP electromagnetic wave interacts with an anisotropic metasurface structure, the output electric field consists of two components. The first component is the original primary polarization state, which has a complex-amplitude of $(t_u + t_v)/2$. The second component is an orthogonal polarization state, corresponding to right-handed polarization for left-handed input (and vice versa), with a complex-amplitude of $(t_u - t_v) \cdot e^{2i\sigma\theta}/2$. Thus, the orthogonal polarization state carries an extra geometric phase of $2\sigma\theta$, induced by the interaction with the metasurface[4]. In other words, the phase modulation induced by the structure is twice the rotation angle of the meta-atom, which is a variable denoted as θ (Supplementary Fig. S1b).

2. Electromagnetic response of an optically addressed meta-atom supercell

The optical addressing process functions as a dynamic switching mechanism to control the activation and deactivation of meta-atoms within a supercell. Within each supercell, individual meta-atoms can be selectively activated or deactivated based on the intensity distribution of the addressing light. This process assumes a binary modulation scheme, wherein the amplitude of selected (active) meta-atoms is assigned a value of 1, while that of unselected (inactive) ones is assigned a value of 0—effectively switching the meta-atoms on or off. This binary control enables dynamic modulation of the output light field: active meta-atoms contribute to the optical response, whereas inactive ones remain non-interactive with the incident light. Supplementary Fig. S2 schematically illustrates the optical addressing process within a pre-discretized meta-atom supercell. The metasurface is discretized into smaller functional units, such as a 2×2 grid, where the addressing light pattern determines the activation state of each meta-atom. High-intensity regions

correspond to active meta-atoms, while low-intensity areas correspond to inactive ones. Through this mechanism, dynamic optical addressing facilitates real-time control of the metasurface, thereby enabling complex light-field modulation governed by the spatial intensity profile applied to the meta-atom supercells.

To model this process, we assume that an optical addressing profile O_l determines whether an *i*-th meta-atom in the supercell is activated or not. Taking a binary switching mechanism, the optical addressing profile O_l can be written as a function:

$$O_l = \begin{cases} 1, & \text{selected meta-atom} \\ 0, & \text{not selected} \end{cases} \tag{S6}$$

When a selected meta-atom is activated, it modulates the incident light by introducing a phase shift proportional to its rotation angle θ_l. According to the discussion above, the modulation of the incident light by each active meta-atom can be described by its Jones matrix and the phase shift $\Delta\varphi_l$ for the *l*-th meta-atom is $\Delta\varphi_l = 2\theta_l$. The corresponding electromagnetic response can be expressed as: $O_l e^{2i\sigma\theta_l}$. The collective effect of the meta-atom supercell on the incident light field can be described by summing the individual contributions of all selected meta-atoms. If there are *a* meta-atoms in the supercell, the collective electromagnetic response of a meta-atom supercell can be expressed as:

$$r = \sum_{l=1}^{a} r_l = \sum_{l=1}^{a} O_l e^{2i\sigma\theta_l} \tag{S7}$$

Taking another view, we assume that the optical addressing profile denotes a matrix as $\boldsymbol{o}$, illuminates a pre-discretized meta-atom supercell with a whole transmission function $\boldsymbol{m}$, which denotes a matrix of electromagnetic response corresponding to each meta-atom. Following propagation through the meta-atom supercell, the global electromagnetic response $\boldsymbol{r}$ describes the phase and amplitude modulation of the light field across the entire metasurface and can be expressed by a matrix product of $\boldsymbol{o}$ and $\boldsymbol{m}$, which allows the modulation to be encoded in the spatial domain.

$$\boldsymbol{r} = \boldsymbol{m} \cdot \boldsymbol{o} \tag{S8}$$

Furthermore, we consider a periodic PDM to consist of an M × N array of meta-atom supercells. The global modulation function of the metasurface represents the total effect of all the meta-atom supercells on the incident addressing light field. It is the sum of the individual contributions from each selected meta-atom supercell, weighted by the activation function (Supplementary Fig. S3). The global electromagnetic response $\boldsymbol{R}$ describes the phase and amplitude modulation of the light field across the entire metasurface and can be expressed as:

$$R = \sum_{m=1}^{M} \sum_{n=1}^{N} r_{m,n} \tag{S9}$$

where $r_{m,n}$ is the Jones matrix for the *i*-th meta-atom. This function encapsulates the collective modulation of the light field due to the selected meta-atom supercells, determining the phase and amplitude modulation across the surface. By adjusting the intensity distribution of the optical addressing profile, the meta-atoms can be selectively

activated or deactivated, changing the global electromagnetic response and thus dynamically controlling the light field. This allows for real-time modulation of the light field, enabling flexible beam-shaping and wavefront manipulation.

Supplementary Note S2. Modulation capacity of an optically addressed meta-atom supercell.

1. Phase-only modulation via discretized meta-atoms

In our method, the optical addressing profiles and the PDM jointly interact through light-matter coupling to enable dynamic spatial light modulation. By predefining discrete phase levels across a full 2π range, when the optical addressing beam selectively illuminates corresponding meta-atoms, pure phase modulation of the wavefront can be achieved (Supplementary Fig. S4). Thus, the basic working principle of the OA-MSLM functions as a pure-phase modulator. We define the number of phase discretization levels as L, and assign to each metasurface unit cell a discrete geometric phase shift given by:

$$\varphi_l = \frac{2\pi l}{L} (l = 0,1,2,\ldots,L-1) \tag{S10}$$

where φ_l denotes the phase imparted by the *l*-th level. Each meta-atom is treated as an independent spatial channel, and different channels are selectively activated by controlling the incident addressing light fields, as defined in Equation(S6). Through this design, the OA-MSLM enables dynamic control of the spatial phase distribution across the aperture. However, since each meta-atom only encodes phase information and lacks amplitude modulation capability, the attainable optical field is limited to phase-only modulation.

2. Complex-amplitude modulation via a superpixel method

To overcome the intrinsic limitation of phase-only modulation and realize full complex-amplitude control, we employ a superpixel-based strategy in which multiple adjacent meta-atoms are grouped to form a functional supercell. As previously discussed, each supercell comprises L neighboring meta-atoms, each imparting a phase response uniformly distributed between 0 and 2π. In the Fourier plane, each pixel's diffraction spot is broadened, causing substantial spatial overlap among adjacent pixels[5,6]. Consequently, the field at the target plane results from the coherent sum of the fields emitted by the constituent meta-atoms. Specifically, the field response of each meta-atom is represented as:

$$E_l = O_l exp(i\phi_l) \tag{S11}$$

where O_l denotes the binary on/off state (depending on the optical addressing), and φ_l is the imparted phase. The total field generated by a superpixel can thus be expressed as:

$$E_{superpixel} = \sum_{l=1}^{L} O_l exp(i\phi_l) \tag{S12}$$

By selectively activating different combinations of meta-atoms within a superpixel, the resulting complex-amplitude $E_{superpixel}$ can be precisely engineered. For example,

activating pixels corresponding to phase shifts of 0, 4π/9, and 8π/9 yields a total field given by the vector sum of these three points in the complex plane (Supplementary Fig. S5g). Therefore, various target fields can be generated by appropriately choosing activation patterns.

In principle, for a superpixel composed of L pixels, up to 2^L distinct activation patterns are possible, significantly enhancing the modulation capacity compared to single-pixel phase-only modulation. Nevertheless, different activation patterns may yield identical resultant fields due to vector sum degeneracy. In this way, we can illustrate the achievable target fields for all possible activation patterns. For a superpixel composed of 4-level discretized meta-atoms, 9 distinct fields can be generated (Supplementary Fig. S5d). For a 9-level discretization, the achievable field capacity dramatically increases to 343 distinct fields, densely and uniformly distributed within a disk in the complex plane (Supplementary Fig. S5h). This uniform distribution allows arbitrary complex-amplitude generation within a small discretization error.

Furthermore, the achievable field set can be stored in a lookup table, enabling any desired normalized complex-amplitude to be mapped to its nearest realizable value. The optical addressing profiles are then encoded accordingly to synthesize a complex-amplitude light field composed of multiple superpixels. This superpixel-based strategy enables independent and simultaneous control over both amplitude and phase, which is essential for advanced applications such as dynamic holography, complex beam shaping, and three-dimensional optical field generation.

Supplementary Note S3. Optical addressing at the meta-atom scale

1. Setup for optical addressing

The optical addressing beam is generated using a custom-designed optical transformation system, as illustrated in Supplementary Fig. S6a. Initially, the laser beam is focused by an objective lens (Daheng, ×40 NA 0.65) and passed through a pinhole (Daheng, GCO-0112M, 25 μm) to eliminate unwanted diffraction artifacts. The filtered beam is subsequently collimated using a lens (Thorlabs, LA1433-A, f =150 mm) to ensure a uniform wavefront and a desired beam size. This expanded beam is then dynamically modulated at high speed using a digital micromirror device (DMD; Texas Instruments, DLP6500FYE), enabling pixel-level control of the optical field. The modulated beam is further processed through a 4f optical system comprising a tube lens (Olympus, SWTLU-C, f =180 mm) and a high numerical aperture objective lens (Olympus, ×20 NA 0.8 or ×10 NA 0.4). Before entering the objective lens, the beam is adjusted to circular polarization through the sequential placement of a linear polarizer (Thorlabs, LPVISA100-MP2) and an achromatic quarter-wave plate (Thorlabs, AQWP10M-580). The pre-patterned metasurface is positioned at the focal plane of the objective lens, where the DMD-controlled optical field is projected with high spatial precision. This setup allows for precise light-addressing capabilities at the level of individual meta-atoms.

Furthermore, the system can be extended into a multi-wavelength light-addressing configuration, as illustrated in Supplementary Fig. S6b. To overcome the varying deflecting angles introduced by the blazed digital mask, multiple beam combiners are positioned in front of the tube lens to merge the light-addressing patterns corresponding to different wavelengths. The combined beam is subsequently focused by the tube lens and the objective lens to generate the desired light-addressing pattern. In this way, independent timing control can be obtained to address and regulate different wavelengths of light. In the experimental implementation, constrained by the cost of the setup, we employed a single digital mask in conjunction with multiple laser sources of different wavelengths. We tested the system with lasers of 633 nm (Pacific Lasertec, 25-LHP-991-230), 532 nm (CNI, MSL-FN-532), and 473 nm (CNI, MBL-III-473-100mW) wavelengths to validate its functionality for corresponding wavelength-specific light addressing.

In addition to the conceptual testing setup, we demonstrated the miniaturization and integration of optically addressed metasurface spatial light modulators, as shown in Supplementary Fig. S7. The previously described optical addressing setup was successfully integrated into a compact module measuring 20×25×15 cm^3, showcasing its potential for applications with strict space constraints. The miniaturized system retains its core functionalities, including beam modulation, polarization control, and high-precision light-addressing at the metasurface level, while achieving a significant reduction in size.

2. Modeling of the optical addressing resolution

The resolution of the optical addressing system is analyzed by simulating the light intensity distribution generated by the propagation of a single longitudinal mode laser through the optical setup. The system adopts a 4*f*-like configuration, comprising a collimating lens and an objective lens, with the digital mask and the metasurface plane designed to be conjugated. To evaluate the light intensity at the focal plane, we employ monochromatic coherent optical models under scalar approximation and paraxial assumptions[7]. The simulation approach models the light propagation in a sequence of steps: a uniform laser beam is first incident on the digital mask, where the field amplitude is modulated by the mask acting as an amplitude filter. The collimating lens then creates an intermediate image of the digital mask at the back focal plane of the objective lens, which subsequently focuses the image onto the metasurface plane to form a highly focused light sheet. This simulation provides precise insights into the spatial resolution of the system and highlights its ability to control the generated light intensity distribution with high accuracy.

Firstly, we introduce the theoretical framework of optical addressing accuracy simulation. The electric field (E_0) of the laser beam that is incident on the DMD surface can be represented as:

$$E_0\left(x_d, y_d\right) = A_0 \tag{S13}$$

Here, x_d and y_d are spatial coordinates on the surface of the DMD, A_0 represents the maximum strength of the electric field.

The field emerging from the DMD (E_d) is given by:

$$E_d\left(x_d, y_d\right) = E_0\left(x_d, y_d\right) H\left(x_d, y_d\right) \tag{S14}$$

Here, the function H has a binary value of 0 or 1 at each spatial coordinate on the DMD surface. Light emerging from the DMD is collected by the collimating lens and then focused by the objective lens. When the DMD surface is located at the focal plane of the collimating lens, the field at the back focal plane of the objective lens (E_B) is obtained through a Fourier transform of the field at the DMD as:

$$E_B\left(x_b, y_b\right) = \frac{1}{i\lambda f_1} \mathcal{F}\left\{E_d\left(x_d, y_d\right)\right\} \tag{S15}$$

Here, f_1 is the focal length of the collimating lens, $i = \sqrt{-1}$ and $\mathcal{F}$ is the Fourier transform operator. The spatial coordinates in the back focal plane of the objective (x_d,y_d) are related to the coordinates on the DMD as:

$$x_b = x_d \frac{\lambda}{f_1}, \quad y_b = y_d \frac{\lambda}{f_1} \tag{S16}$$

The field propagating into the back aperture of the objective lens (E_A) is limited by the pupil function (P) of the objective as:

$$E_A\left(x_b, y_b\right) = E_B\left(x_b, y_b\right) P\left(x_b, y_b\right) \tag{S17}$$

The pupil function depends on the diameter of the circular back aperture of the objective lens (D_{obj}) and is given by:

$$P\left(x_b, y_b\right) = \begin{cases} 1 \text{ for } \left|\sqrt{x_b^2 + y_b^2}\right| < 0.5 D_{obj} \\ 0.5 \text{ for } \left|\sqrt{x_b^2 + y_b^2}\right| = 0.5 D_{obj} \\ 0 \text{ for } \left|\sqrt{x_b^2 + y_b^2}\right| > 0.5 D_{obj} \end{cases} \tag{S18}$$

The field in the focal plane of the objective lens (E_f) is obtained by propagating the field through a thin lens as:

$$E_f\left(x_f, y_f, z_f\right) = \frac{n}{i\lambda f_2} \exp\left(\frac{2\pi i\left(2f_2 + z_f\right)}{\lambda / n}\right) \mathcal{F}\left\{E_A\left(x_b, y_b\right) \exp\left(-\frac{2\pi i\left(x_b^2 + y_b^2\right)}{\lambda f_2 / n} \frac{z_f}{f_2}\right)\right\} \tag{S19}$$

Here, n is the refractive index of the immersion medium of the objective lens, f_2 is the focal length of the objective lens and z_f is the axial coordinate along the propagation direction with its origin at the focal plane of the objective. At the focal plane (i.e., at $z = 0$), Equation(S19) reduces to a Fourier transform of the field at the back aperture of the objective (E_A) with a constant phase pre-factor. The lateral coordinates $x_f = Mx_d$ and $y_f = My_d$ are related to the spatial coordinates on the DMD surface through the optical magnification of the system ($M = f_2/f_1$).

Finally, the intensity in the focal plane (I_f) is obtained from the electric field as:

$$I_f\left(x_f, y_f, z_f\right) = \left|E_f\left(x_f, y_f, z_f\right)\right|^2 \tag{S20}$$

3. Simulation of the intensity distribution during optical addressing

Based on the established theoretical framework, a numerical simulation model was constructed in MATLAB to evaluate the spatial resolution achievable through single-pixel optical addressing. Equations(S13)-(S20) were numerically implemented, with the Fourier transform operations carried out using MATLAB's built-in 'fft2()' function to model the propagation of the optical fields in the system. The primary objective of the simulation was to assess whether individual pixels on the digital mask could independently and precisely address corresponding meta-atoms on the metasurface, a critical requirement for achieving high-fidelity dynamic modulation. Specifically, the addressing spot size at the metasurface plane was characterized by calculating the full width at half-maximum (FWHM) of the intensity profile under single-pixel illumination.

Simulations were performed for three representative visible wavelengths, 473 nm, 532 nm, and 633 nm, to cover the typical operating range of the system. As shown in Supplementary Fig. S8, the calculated FWHM values were 331 nm, 362 nm, and 425 nm for 473 nm, 532 nm, and 633 nm, respectively. These results indicate that the optical addressing resolution remains below the sub-micron scale across the visible spectrum, validating the theoretical feasibility of meta-atom-level independent addressing. As shown in Supplementary Fig. S9, as the number of activated pixels increases, the width of the projected spot at the target plane shows a near-linear growth, demonstrating the controllable scalability of the addressing beam size through pixel number modulation. These results confirm the feasibility of dynamic beam shaping with pixel-level precision using the optical addressing approach.

Supplementary Note S4. Characterization of the optical addressing performance.

1. Setup for spatial resolution characterization

The spatial resolution of the optical addressing system was experimentally evaluated to determine the minimum distinguishable addressed spot size, as shown in Supplementary Fig. S10. A high-magnification imaging system equipped with a CMOS camera (MER-2000-19U3MC-L, Daheng Imaging; pixel size: 2.4 μm × 2.4 μm) was employed. The optical setup included a ×100 air objective lens (MPLAPON ×100, Olympus; NA = 0.95) and a tube lens (TTL100-A, Thorlabs; focal length = 100 mm; working distance = 63.1 mm). Gaussian fitting was applied to the intensity distributions of the optical addressing spots corresponding to single-pixel illumination to extract their FWHM values.

2. Spatial resolution of the optical addressing setup

Following the setup described above, experimental characterization of the spatial resolution was performed to evaluate the achievable optical addressing precision. A digital mask was employed to generate pixel-based addressing patterns, which were projected onto the metasurface plane through the optical system. Two basic addressing modes were tested: single-pixel addressing and interval-pixel addressing, as illustrated in Supplementary Fig. S11a, d, respectively. The digital mask featured a pixel pitch of 7.56 μm. Numerical simulations based on the optical setup parameters were conducted to predict the focal plane

intensity distributions for both addressing modes. The *x*-*y* plane intensity profiles were obtained through Fourier optics modeling using the pixelated input patterns (Supplementary Fig. S11b, e). Experimentally, the projected addressing spots were captured at the focal plane using the high-NA objective and CMOS imaging system described previously. As shown in Supplementary Fig. S11c, f, the experimentally measured intensity profiles are in good agreement with the simulation results.

For the single-pixel addressing pattern at an incident wavelength of 532 nm, the simulated and experimental FWHM values were 362 nm and 371.1 nm, respectively. For the interval-pixel addressing pattern, the simulated and experimental peak-peak intervals were 756 nm and 759.3 nm, respectively. The close match between simulation and experiment validates the accuracy of the optical modeling and confirms that the optical addressing system achieves subwavelength focusing performance for single-pixel excitation, as well as predictable spot broadening for multi-pixel configurations.

3. Optical addressing demonstration for 4-level and 9-level PDMs

Building upon the single-pixel optical addressing characterization, we further evaluated the performance of optical addressing for pre-discretized metasurface templates (PDMs) composed of multi-level meta-atom supercells. Specifically, 4-level and 9-level discretization schemes were tested to verify the ability of the optical addressing system to selectively activate individual meta-atoms within a supercell structure.

For the 4-level PDM, two addressing patterns were designed to target 16 and 64 meta-atom supercells, respectively (Supplementary Fig. S12a, d). Each supercell contained four meta-atoms, each corresponding to a discrete phase level spanning 2π. Optical addressing beams were programmed to selectively illuminate specific meta-atoms within each supercell, enabling controlled modulation of the spatial phase distribution. The simulated and experimentally measured intensity profiles at the focal plane (Supplementary Fig. S12b, c, e, f) show excellent agreement, confirming accurate and localized optical excitation at the meta-atom level.

Similarly, for the 9-level PDM, optical addressing patterns were designed for 16 and 64 supercells, where each supercell consisted of nine meta-atoms (Supplementary Fig. S13a, d). The addressing scheme allowed for selective illumination among nine pre-discretized phase levels, greatly enhancing the modulation flexibility. The corresponding simulated and measured intensity profiles (Supplementary Fig. S13b, c, e, f) demonstrate high-fidelity addressing performance, validating the scalability of the optical addressing strategy to higher discretization levels.

These results collectively demonstrate that the developed optical addressing system can reliably achieve subwavelength, meta-atom-level selective activation across different discretization schemes, paving the way for dynamic complex-amplitude wavefront modulation.

4. Temporal resolution of the optical addressing setup.

The temporal resolution of the optical addressing system for the OA-MSLM was characterized to determine its maximum achievable frame rate. As illustrated in Supplementary Fig. S14a, the experimental setup employed a fast photodiode (DET025A/M, Thorlabs) with a bandwidth of 2 GHz and rise/fall times of approximately 150 ps, covering a spectral range of 400–1100 nm. The photodiode output was recorded by a high-speed oscilloscope (InfiniiVision DSO-X 3104A, Agilent Technologies) featuring a 5 GSa/s sampling rate, 4 GHz analog bandwidth, and 50 Ω input impedance. To generate time-varying optical addressing patterns, voltage signals from a signal generator were used to modulate the digital mask. The dynamically generated optical patterns were subsequently projected onto the metasurface via the optical addressing system. The temporal response was characterized by synchronously controlling the switching signals applied to the digital mask and recording the resulting variations in optical power detected by the photodiode. Supplementary Fig. S14b presents the temporal response over multiple switching cycles, where the yellow curve corresponds to the applied voltage signal, and the green curve corresponds to the detected optical power. Supplementary Fig. S14c further shows the detailed response to a single switching event, yielding a measured rise time of 2.8 μs and a fall time of 0.45 μs. The measured switching time for one frame was 77 μs, corresponding to a maximum achievable operating frequency of approximately 12.987 kHz. These results confirm the capability of the optical addressing system to support high-speed dynamic modulation at kHz frame rates.

Supplementary Note S5. Design and fabrication of the pre-discretized metasurface.

1. Simulation and optimization of the meta-atom structure

To ensure general applicability, titanium dioxide (TiO_2) anisotropic nanobricks are employed to form a supercell and modulate circularly polarized light based on the geometric phase (Supplementary Fig. S15). Under circularly polarized incidence, each meta-atom generates orthogonally polarized transmitted light with an additional phase. The feature size was optimized to achieve a high polarization conversion efficiency, defined as the ratio of the transmitted power of orthogonally polarized light to the power of the incident circularly polarized light. The refractive index of TiO_2 across the visible spectrum (400–800 nm), used as input for the simulations, is plotted in Supplementary Fig. S15b. The period of a single meta-atom was set at 378 nm, balancing the projection relationship and fabrication capabilities. The electromagnetic response of the meta-atoms was analyzed by sweeping the length and width of the nanobricks (with a fixed height of 700 nm and period of 378 nm) using the commercial simulation software CST Microwave Studio, as shown in Supplementary Fig. S15c. After optimization, the meta-atom dimensions were determined to be 250 nm in length and 100 nm in width, considering fabrication constraints. The polarization conversion ratio of the optimized meta-atom was simulated across the visible wavelength range (400–800 nm), with particularly high performance at the working wavelengths of 473 nm, 532 nm, and 633 nm, as shown in Supplementary Fig. S15e.

2. Impact of the coupling and phase discretization

To analyze the impact of near-field coupling within a supercell, a 4-level meta-atom supercell comprising meta-atoms oriented at -45°, 0°, 45°, and 90° was modeled (Supplementary Fig. S16a). The simulated normalized amplitude of the electric fields under LCP illumination is shown in Supplementary Fig. S16b. The cross-sectional cutting planes (S1–S4) are indicated by black dashed lines in the top view. The results show that the electric fields are well-confined inside and around the high-index dielectric meta-atoms, with negligible near-field coupling between adjacent elements. Consequently, the four meta-atoms function effectively as independent birefringent waveplates, facilitating controlled far-field interference. The phase delays induced by different in-plane rotation angles agree well with theoretical predictions based on the PB geometric phase. Since the coupling between meta-atoms is negligible, the electromagnetic response of the meta-atom supercells can be treated as a vector superposition of the responses of individual meta-atoms. These meta-atoms are selectively activated using the optical addressing strategy. The simulated electromagnetic response when selectively addressing a single meta-atom within a 4-level meta-atom supercell is shown in Supplementary Fig. S17a, b. Compared with the ideal geometric phase, the positional deviation of the meta-atom has a negligible effect on the phase response. Specifically, for the 4-level meta-atom supercell, the deviation is approximately one-twentieth of the designed geometric phase interval, while for the 9-level meta-atom supercell (Supplementary Fig. S17c, d), the deviation increases to about one-quarter of the interval. Furthermore, since both the incident angle and observation angle are 0°, the detour phase effect is negligible and not considered in this design.

3. Fabrication process of the dielectric metasurface.

The fabrication process of the TiO_2 metasurfaces is illustrated in Supplementary Fig. S18. The metasurfaces were fabricated using a combination of electron beam lithography (EBL) and reactive ion etching (RIE). The process began with spin-coating a 200 nm-thick layer of PMMA resist onto a 700 nm-thick TiO_2 film deposited on a SiO_2 substrate. The PMMA layer was then patterned via EBL to define the nanoscale structures. After development in an IPA solution, nanostructures were formed in the resist. Subsequently, a 28 nm-thick chromium (Cr) layer was deposited onto the patterned resist using an electron beam evaporator. A lift-off process was then performed to define the Cr hard mask. The underlying TiO_2 film was etched using Cl_2 and C_4F_8 gases in an RIE to transfer the pattern into the TiO_2 layer. Finally, the Cr mask was removed by wet etching, leaving behind the fabricated TiO_2 metasurface nanostructures with high fidelity. Following the fabrication process, metasurface samples with different meta-atom supercell configurations were realized, as shown in Supplementary Fig. S19. Samples were fabricated featuring 4-level and 9-level pre-discretized meta-atom supercells, as well as a double 4-level configuration for enhanced spatial multiplexing. Each meta-atom supercell arrangement was designed to facilitate spatial phase modulation through geometric phase control.

Supplementary Note S6. Demonstration of dynamic holographic display.

In this section, we demonstrate a series of dynamic holographic displays based on the OA-MSLM. Various types of holographic displays, including far-field Fourier holography, near-

field Fresnel holography, multi-layer Fresnel holography, complex-amplitude holography, and dual display combining nanoprinting and holography, are explored. These demonstrations showcase the versatility, broadband performance, and dynamic capabilities of the OA-MSLM platform.

1. Workflow framework for dynamic holographic display

A systematic workflow was established to realize dynamic holographic displays using the OA-MSLM. The process begins with the definition of a target image, such as the “HUST” logo pattern (Supplementary Fig. S20a). To reconstruct the desired optical field, a hologram design algorithm based on inverse fast Fourier transform (iFFT) is employed, which transforms the target image into a corresponding complex electromagnetic field distribution. In the case of phase-only holography, the phase component is extracted to generate a continuous phase distribution (Supplementary Fig. S20b), which is then mapped onto the optically addressed PDM. This mapping strategy enables the encoding of various holographic functions, including phase-only and complex-amplitude holograms. Depending on the design requirements, additional algorithms, such as Gerchberg–Saxton (GS) iteration or stochastic gradient descent (SGD)-based optimization, can be incorporated to refine the electromagnetic profile or enhance image fidelity.

To match the constraints of the physical metasurface structure, the continuous phase profiles are discretized according to the predefined meta-atom supercell arrangement, forming an addressing map (Supplementary Fig. S20c). This discretization enables dynamic spatial wavefront modulation through the optical addressing system. The generated optical addressing pattern for a 4-level pre-discretized metasurface is shown in Supplementary Fig. S20d, serving as the modulation input for dynamic holography. Supplementary Fig. S20e presents the simulated holographic reconstruction based on the optically addressed metasurface, validating the feasibility of the proposed approach.

2. Far-field Fourier holographic display

Fourier holography operates in the far field, where the optical field distribution corresponds to the Fourier transform of the metasurface's transmission function. It enables high-resolution, wide-field imaging by encoding the target patterns in the angular spectrum domain. In this configuration, holographic images are reconstructed at the focal plane of a Fourier lens without direct imaging optics. The far-field Fourier holographic display was experimentally demonstrated using the OA-MSLM at working wavelengths of 532 nm and 473 nm. As shown in Supplementary Fig. S21, holographic reconstructions of 10 Arabic numerals and 26 English letters were successfully achieved. Dynamic holographic displays were further realized by sequentially updating the optical addressing patterns to depict the evolution of the Chinese character "光" ("light") over historical periods, as depicted in Supplementary Fig. S22a. Six representative character styles from different eras were selected. The corresponding measured holographic images at 473 nm and 532 nm are shown in Supplementary Fig. S22b, c, demonstrating dynamic and high-speed switching performance. The dynamic animation sequences of the far-field Fourier holographic display,

showing continuous evolution of holographic images, can be found in Supplementary Movie S1.

3. Near-field Fresnel holographic display

Fresnel holography reconstructs optical fields in the near field, where the light propagation can be described by Fresnel diffraction. Unlike Fourier holography, Fresnel holography provides flexible control over image size, position, and depth, making it ideal for compact and broadband dynamic displays. Near-field Fresnel holography was implemented on the OA-MSLM platform. As shown in Supplementary Fig. S23, holographic images of 10 Arabic numerals and 26 English letters were captured at working wavelengths of 633 nm, 532 nm, and 473 nm, demonstrating broadband operational capability. Dynamic Fresnel holography of the evolving Chinese character "光" was also performed. The measured dynamic reconstructions at different wavelengths are shown in Supplementary Fig. S24b-d, confirming broadband, dynamic near-field imaging with high fidelity. The dynamic animation sequences of the near-field Fresnel holographic display, showing continuous evolution of holographic images, can be found in Supplementary Movie S2.

4. Multi-layer Fresnel holographic display

Multi-layer Fresnel holography was demonstrated to further expand the dynamic capability. As shown in Supplementary Fig. S25a, two distinct images ("A" and "B") were simultaneously encoded at axial planes of 1500 μm and 2000 μm using a modified Fresnel Gerchberg-Saxton algorithm. The corresponding phase profiles and optical addressing patterns are presented in Supplementary Fig. S25b, c. Simulated and experimental reconstructions (Supplementary Fig. S25d, e) confirm the independent reconstruction of multi-depth images, demonstrating depth-encoded dynamic holography. The dynamic animation sequences of the multi-layer Fresnel holographic display, showing continuous evolution of holographic images, can be found in Supplementary Movie S3.

5. Complex-amplitude Fresnel holographic display

Traditional phase-only holography limits the reconstruction fidelity due to the lack of amplitude control. Complex-amplitude holography simultaneously modulates both the amplitude and phase of the light field, enabling higher reconstruction accuracy, enhanced dynamic range, and more flexible wavefront shaping. The frameworks of phase-only and complex-amplitude holography are compared in Supplementary Fig. S26. In complex-amplitude holography, the optical addressing patterns independently control both the amplitude and phase distributions of the meta-atom supercells, significantly improving the modulation capability. Experimental demonstrations of complex-amplitude holography at 532 nm and 473 nm are shown in Supplementary Fig. S27, achieving improved image quality compared to phase-only approaches. Dynamic reconstructions of the Chinese character "光" under complex-amplitude encoding are shown in Supplementary Fig. S28, confirming the enhanced flexibility and precision of the technique. The dynamic animation sequences of the complex-amplitude Fresnel holographic display, showing continuous evolution of holographic images, can be found in Supplementary Movie S4. A comparison

of holographic displays reconstructed from POH and CAH is provided in Supplementary Fig. S29, Fig. S30 and Movie S5.

6. Dual display of nanoprinting and holographic image.

To increase the information density and multifunctionality of metasurface-based displays, a dual display mode combining grayscale nanoprinting and dynamic holography was demonstrated. By simultaneously encoding distinct optical functionalities at different planes, more complex and richer information presentation can be achieved within a single compact device. This dual functionality is enabled by the complex-amplitude modulation capability of the OA-MSLM, where both the amplitude and phase of the optical field can be independently controlled. Unlike traditional phase-only modulation, complex-amplitude modulation allows precise tailoring of the light field at multiple planes, enabling the concurrent generation of near-field grayscale amplitude images and far-field holographic projections. This significantly enhances the multifunctional display capabilities and application flexibility of metasurface platforms. The experimental implementation is shown in Supplementary Fig. S31. In this setup, a metasurface was illuminated with an amplitude pattern ("Einstein") representing a grayscale sphere at the metasurface plane. Simultaneously, holographic images (the kinetic energy equation) were encoded at an object plane located 2 mm away. Supplementary Fig. S31a presents the system schematic. Fig. S31B, C illustrate the encoded amplitude and phase profiles and the optical addressing pattern applied to the 9-level pre-discretized metasurface. Simulated and experimentally measured reconstructions of both the grayscale amplitude image and the holographic image are shown in Supplementary Fig. S31d–i, demonstrating broadband, multifunctional optical field manipulation. The dynamic evolution of the focusing plane along the *z*-axis can be found in Supplementary Movie S6, illustrating the dual display of an amplitude pattern and a holographic image.

Supplementary Note S7. Demonstration of 3D focusing.

In this section, we demonstrate the capability of the OA-MSLM for 3D light field control. Various types of 3D focusing and point-based holographic displays are achieved, including single focal focusing, dynamic planar focal scanning, planar multi-focal spot generation, point-element-based holographic display, and 3D spiral focusing. These demonstrations highlight the versatility of the OA-MSLM in manipulating complex 3D optical fields, offering promising applications in optical tweezers, volumetric displays, and 3D optical lithography.

1. Single focal focusing

Single focal focusing refers to the concentration of light into a tightly confined spot at a designated axial position. By encoding a spherical phase profile onto the OA-MSLM, constructive interference leads to the formation of a diffraction-limited focal point. This technique serves as the basic functionality for various 3D light manipulation applications. Supplementary Fig. S32 illustrates the working principle and experimental results of single focal focusing. The target phase profile was generated based on the desired focal length f,

working wavelength λ, and pixel period *Lp*, and then converted into an optical addressing pattern. Measured intensity distributions along the propagation direction show the expected focusing behavior. The intensity profiles at the metasurface plane (z = 0 μm) and at the focal plane (z =1145 μm) confirm successful focusing. The lateral and axial intensity profiles quantitatively validate the focusing performance.

2. Dynamic planar focal scanning

Dynamic planar focal scanning involves shifting the focal spot across different lateral positions at a fixed axial plane. By dynamically updating the optical addressing patterns, rapid lateral scanning of the focused spot can be achieved, which is essential for applications like laser scanning microscopy and optical data storage. Supplementary Fig. S33 presents the principle and results of dynamic planar focal scanning. Target phase profiles corresponding to different lateral positions were sequentially generated and projected onto the pre-discretized metasurface. Simulated intensity distributions and measured results at 473 nm and 532 nm confirm the successful generation and scanning of planar focal spots.

3. Planar multi-focal spot generation.

Planar multi-focal spot generation enables the simultaneous formation of multiple focal spots at the same axial plane. By encoding multiple spherical phase terms into a single addressing profile, an array of foci can be produced, which is important for parallel optical trapping and multi-site manipulation. Supplementary Fig. S34 shows the simulation and experimental results of multi-focal spot generation. Phase profiles for 3×3, 4×4, and 5×5 grids were encoded onto the optical addressing beams. Measured multi-focal spot patterns match well with the simulated designs, demonstrating accurate control over spot formation.

4. Point-element-based holographic display.

Point-element-based holography utilizes arrays of individually focused points to reconstruct arbitrary holographic images. Each point acts as a discrete source contributing to the overall image through Fresnel diffraction. Supplementary Fig. S35 demonstrates the static point-based holographic display of 10 Arabic numerals and 26 English letters at working wavelengths of 532 nm and 473 nm. Dynamic display sequences of the evolving Chinese character "光" are presented in Supplementary Fig. S36, confirming the capability for dynamic holographic switching. The dynamic animation sequences of the point-element-based holographic display, showing continuous evolution of holographic images, can be found in Supplementary Movie S7.

5. Generation of 3D focusing along a spiral line

3D spiral focusing involves arranging focal points along a spiral trajectory in three-dimensional space. This structure can be engineered by combining radial and axial phase modulations, enabling applications in 3D optical trapping, micromanipulation, and 3D printing. Supplementary Fig. S37 shows the schematic design, phase profile generation, and experimental verification of spiral focusing. Target phase profiles were designed to form a 32-point spiral with a radius of 50 μm and a screw pitch of 500 μm, with the first focal point positioned at a distance of 2 mm along the *z*-axis. Simulated and measured reconstructions

confirm the successful generation of the spiral 3D light field at 473 nm and 532 nm. The dynamic evolution of the spiral focusing along the *z*-axis can be found in Supplementary Movie S8, illustrating the continuous movement of focal points along the helical path.

Supplementary Note S8. Demonstration of dynamic beam steering.

In this section, we demonstrate the capability of the OA-MSLM for dynamic beam steering. Various types of beam deflection operations are realized, including maximum deflection angle testing and two-dimensional patterned beam steering. A comparative analysis with state-of-the-art approaches is also conducted. These demonstrations highlight the advantages of the OA-MSLM in achieving broadband, large-angle, and high-resolution optical steering.

1. Calculation of beam deflection angles

Beam steering in a metasurface system is achieved by imposing a linear phase gradient across the aperture, which is equivalent to forming a blazed diffraction grating. The outgoing beam deflection is governed by the generalized Snell's law, where the deflection angle θ_T satisfies[1]:

$$sin(\theta_T) = \frac{\lambda}{2\pi}\frac{d\phi}{dx} \tag{S21}$$

where λ is the working wavelength, $d\phi/dx$ is the spatial phase gradient across the metasurface.

In practical metasurface implementations, the phase profile is discretized with a pixel pitch p and a defined number of phase levels. For a uniformly periodic phase ramp covering 2π over a spatial period Λ, the deflection angle follows the grating equation:

$$sin(\theta_T) = \frac{\lambda}{\Lambda} \tag{S22}$$

where the effective grating period Λ is determined by:

$$\Lambda = N \times p \tag{S23}$$

with N being the number of pixels used to span a full 2π phase shift. Thus, the deflection angle can be rewritten as:

$$sin(\theta_T) = \frac{\lambda}{Np} \tag{S24}$$

To achieve the largest deflection angle, a π phase difference is introduced between adjacent pixels[8]. In this case, two pixels form one grating period (Λ=2p), leading to the maximum deflection angle:

$$\theta_{T,max} = arcsin(\frac{\lambda}{2p}) \tag{S25}$$

For the OA-MSLM developed in this work, the pixel size for the 4-level PDM is 756 nm. Taking a wavelength of 532 nm as an example, the maximum theoretical deflection angle

using a two-pixel period (Λ=1.512 μm) is estimated to be 20.60°, corresponding to a field of view (FOV) of ±20.60°. The FOV could be further extended by employing longer working wavelengths while maintaining the same optical addressing design.

The maximum deflection angle and pixel resolution are thus critical metrics for evaluating the performance of beam steering systems. A comparative analysis between the OA-MSLM and conventional 2D beam steering technologies, including traditional SLMs, DMDs, and metasurface-based SLMs, is summarized in Supplementary Fig. S38. In particular, the experimentally measured maximum deflection angle at 532 nm is indicated by a red star symbol for direct comparison.

2. Beam deflection and maximum scanning angle characterization

Beam steering refers to the controlled redirection of an optical beam without mechanical movement, typically achieved by introducing a spatial phase gradient across the wavefront. In metasurface-based devices, discrete phase shifts emulate gratings with varying periods, enabling beam deflection at designed angles. The maximum achievable deflection angle depends on the pixel size, phase discretization, and working wavelength. Supplementary Fig. S39 presents the characterization of beam deflection using the OA-MSLM. Target phase profiles were generated by designing periodic phase gradients across the metasurface, which were then mapped into corresponding optical addressing patterns. By varying the phase gradients, specifically by adjusting the number of pixels used to cover one grating period, dynamic control of beam steering was achieved. Experimental verification was conducted for modulation periods of 2p, 4p, and 8p, where p is the pixel pitch of meta-atom supercells. The measured deflection angles show good agreement with the theoretical predictions.

3. 2D patterned beam deflection

2D patterned beam deflection extends single-point beam steering to the controlled formation of arbitrary spatial beam patterns in the far field. By dynamically updating local phase gradients across the metasurface, complex 2D scanning patterns, such as letters or logos, can be synthesized without any mechanical movement. Supplementary Fig. S40 presents the experimental results of patterned beam steering using the OA-MSLM. Target phase profiles corresponding to scanned patterns, including a handwritten "W" and a "HUST" logo, were generated by distributing discrete beam directions over the desired angular coordinates and encoding them into optical addressing patterns. The resulting beam patterns, reconstructed by stacking the maximum intensity values from each scanned position, are shown in Supplementary Fig. S40a–c for the "W" pattern and in Supplementary Fig. S40d–f for the "HUST" logo. These results demonstrate the ability of the OA-MSLM to realize dynamic and flexible two-dimensional beam steering with high fidelity. A dynamic animation illustrating the sequential formation of the scanned beam patterns is provided in Supplementary Movie S9.

Supplementary Figures

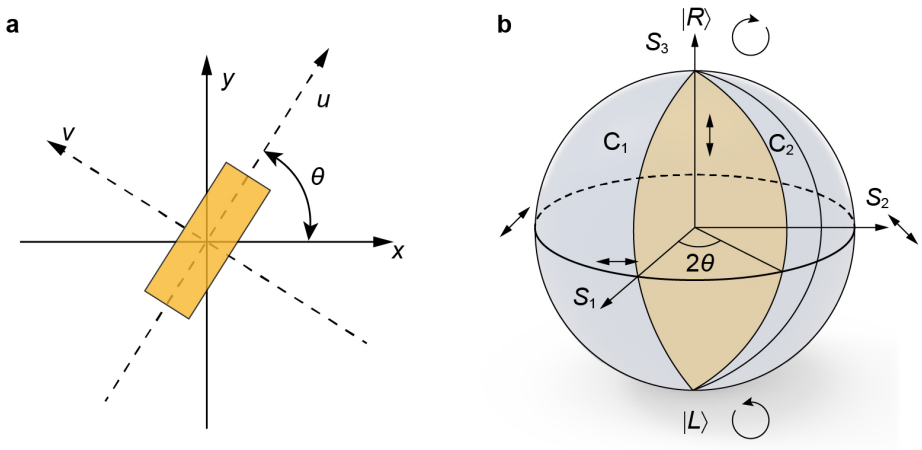

Fig. S1 Illustration of the principle of geometric phase.

(a) Local coordinate system of an anisotropic meta-atom. (b) Geometric phase principle illustrated using the Poincaré sphere.

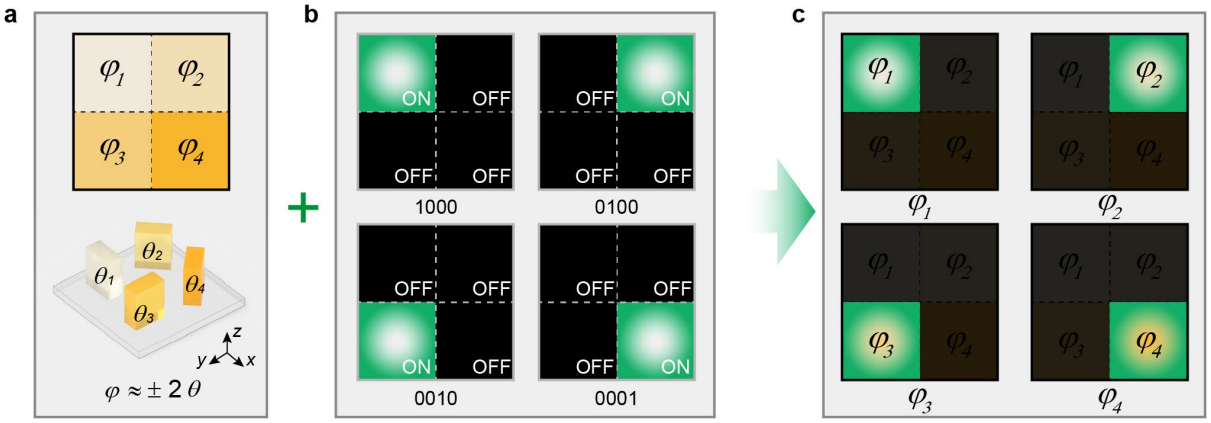

Fig. S2. Principle of optical addressing within a pre-discretized meta-atom supercell.

(a) Detailed configuration of a 4-level pre-discretized meta-atom supercell. (b) Schematic of the optical addressing pattern used to activate the meta-atom supercell. Four individual optical channels can each be turned “on” or “off.” (c) Output response of the optically addressed meta-atom supercell. By selectively activating different subsets of meta-atoms, various functional responses can be achieved within a single device. Leveraging the four discrete phase levels, a 4-level phase modulation capability is realized.

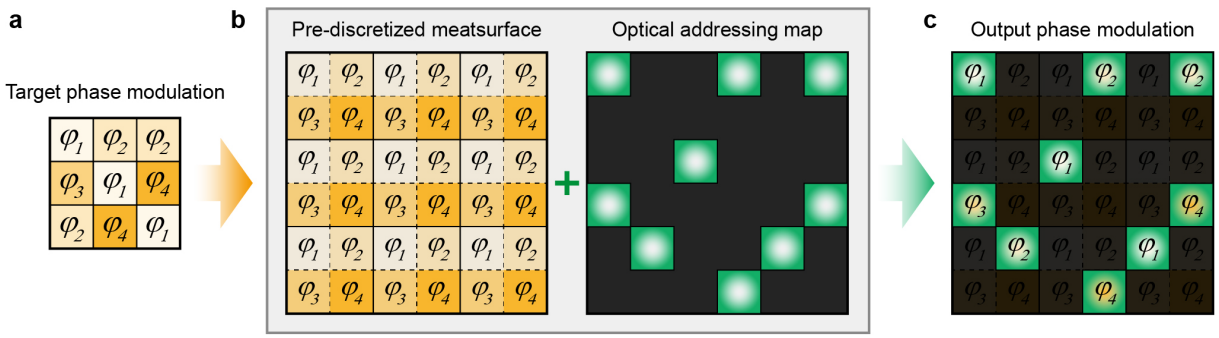

Fig. S3. Generalized workflow of OA-MSLM for dynamic phase modulation.

(a) Target phase modulation. (b) Illustration of a 4-level PDM along with its corresponding optical addressing map for target phase modulation. (c) Resulting phase modulation achieved by optical addressing the PDM. By leveraging the PDM structure, arbitrary target phase distributions can be generated simply by updating the optical addressing pattern. When the target phase distribution changes, updating this pattern enables rapid and dynamic reconfiguration of the output wavefront, thus providing a versatile platform for real-time wavefront shaping.

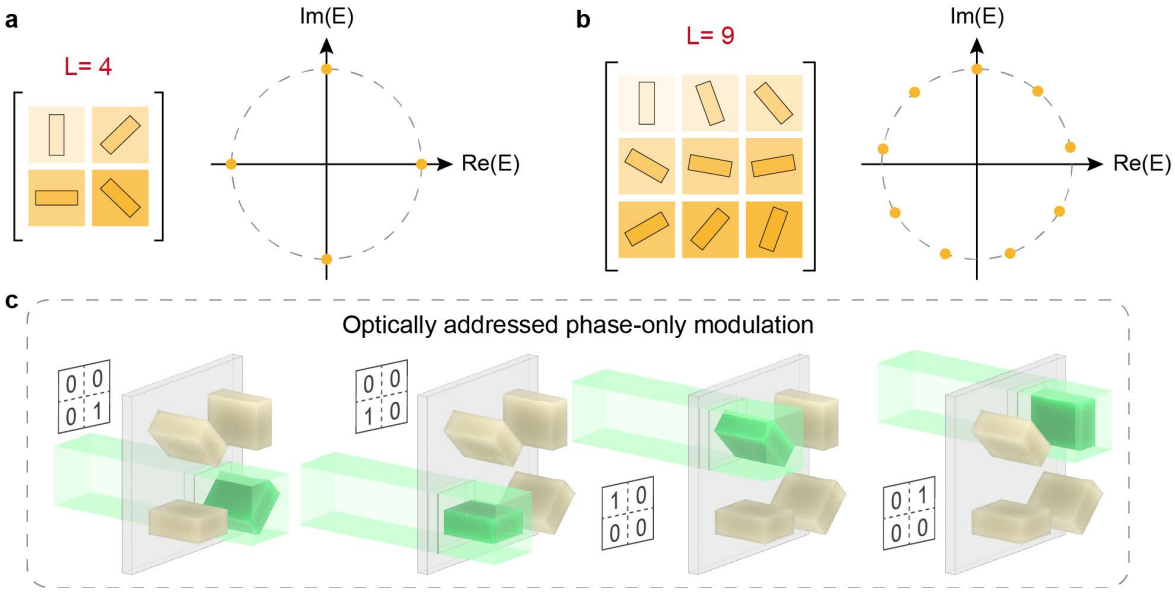

Fig. S4. Optically addressed phase-only modulation.

(a) Illustration of a 4-level discretized meta-atom supercell. (b) Illustration of a 9-level discretized meta-atom supercell. The target plane responses of the sub-meta-atoms that make up a superpixel are then uniformly distributed over a circle in the complex plane. (c) Illustration of the optical addressing process for a 4-level phase-only modulation.

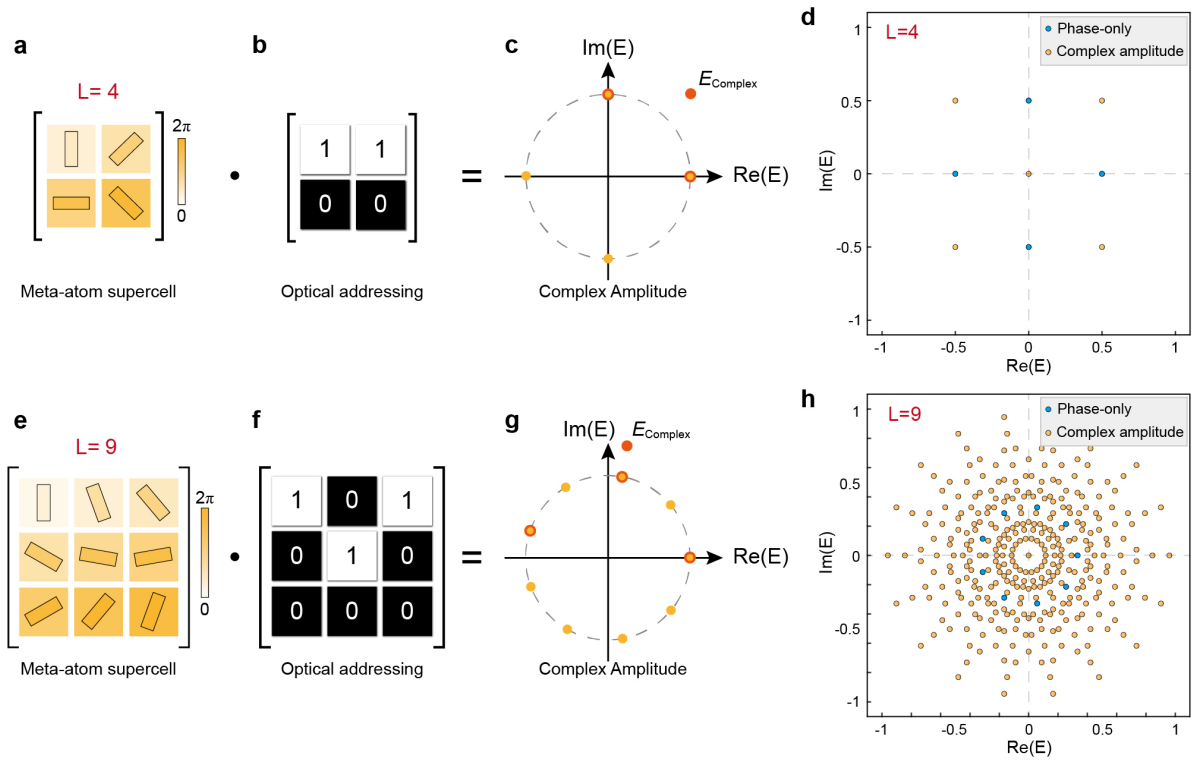

Fig. S5. Optically addressed complex-amplitude modulation.

(a, e) Periodic phase masks for 4-level and 9-level discretized meta-atom supercells. (b, f) Binary optical addressing profiles, with white indicating the "on" state and black indicating the "off" state. (c, g) Resulting complex-amplitude fields generated by different combinations of phase values. (d) Achievable target fields from a single 4-level superpixel (9 distinct fields). (h) Achievable target fields from a single 9-level superpixel (343 distinct fields). The fields marked in blue correspond to selections within a specified amplitude interval, illustrating pure-phase modulation as an example.

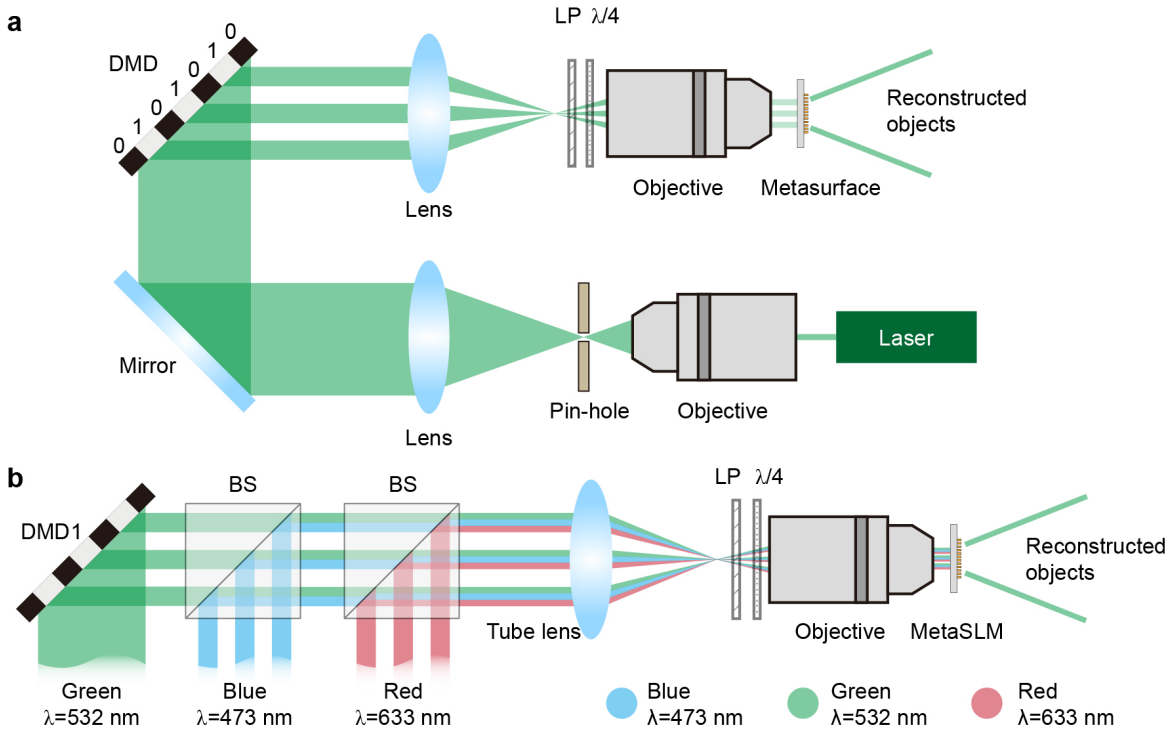

Fig. S6. Schematic of the setup for optical addressing.

(a) The laser beams are processed through a pinhole to remove diffraction artifacts, collimated, and dynamically modulated by a digital micromirror device. A 4*f* system with polarization control ensures precise projection of the modulated beam onto the metasurface. (b) For multi-wavelength addressing, beam combiners merge light patterns of different wavelengths at 633 nm (red), 532 nm (green), and 473 nm (blue), which are then focused to achieve wavelength-specific light addressing at the metasurface plane.

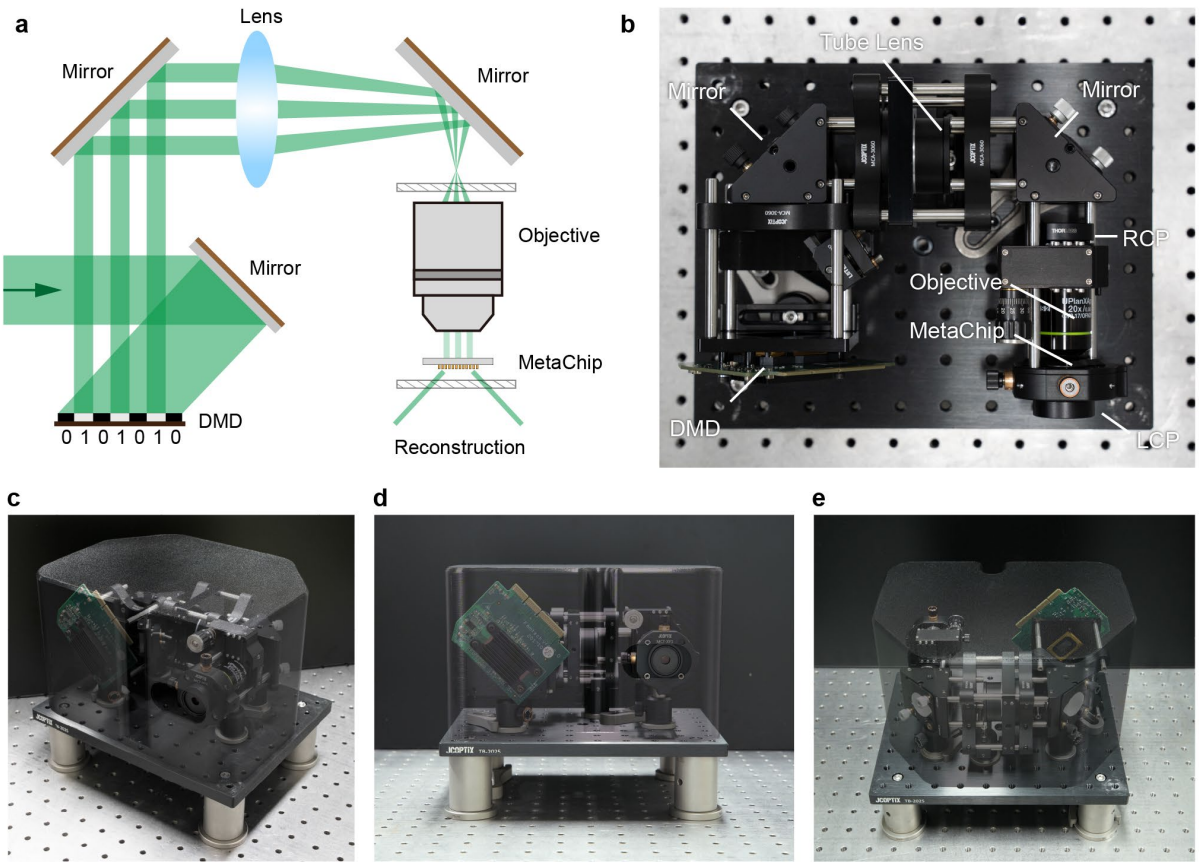

Fig. S7. Miniaturized optical addressing setup.

(a) Schematic of the integrated optical path. (b) Photograph of the assembled structure of the miniaturized system. Side view (c), front view (d), and angled top-down view (e) of the compact optical addressing module.

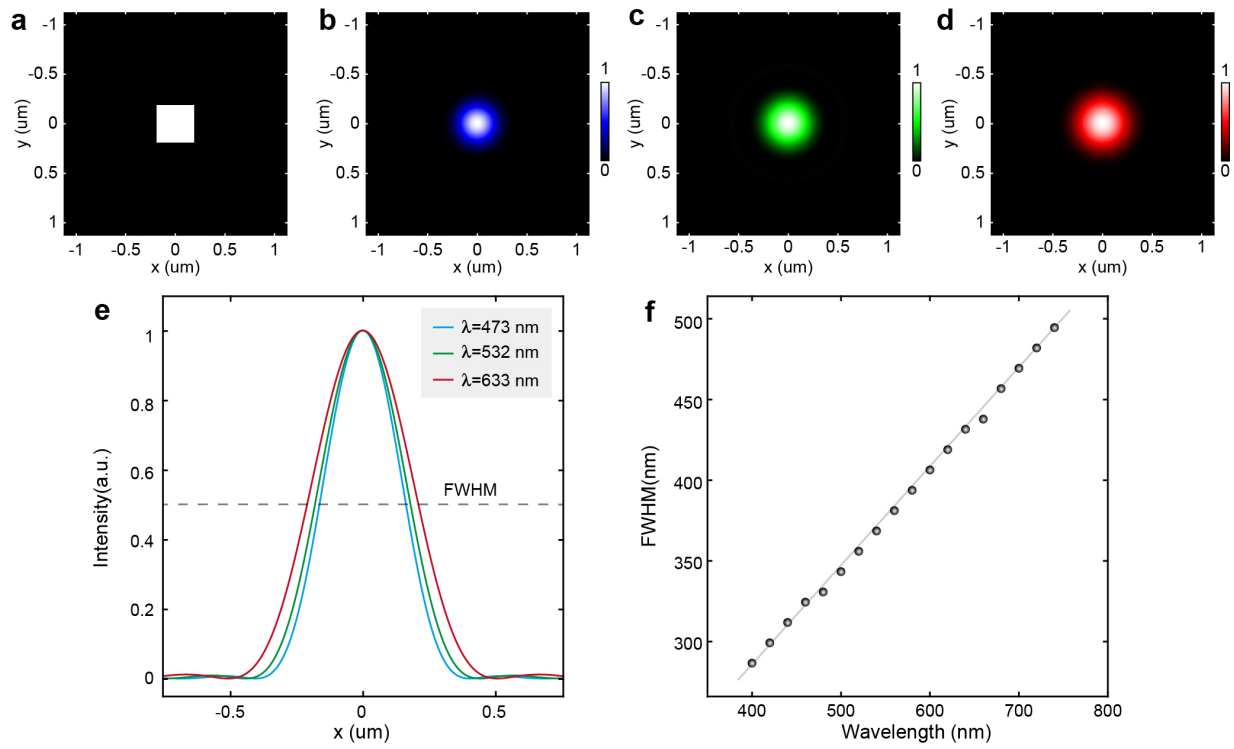

Fig. S8. Simulated spatial resolution of pixel-based optical addressing.

(a) A single-pixel pattern is projected onto the digital mask, representing the fundamental addressing unit. (b-d) Simulated intensity distributions in the x-y plane at the focal plane of the optical addressing system for input laser wavelengths of 473 nm, 532 nm, and 633 nm, respectively. (e) Lateral intensity profiles extracted from (b-d), with FWHM values of the single-pixel addressing patterns measured as 331 nm, 362 nm, and 425 nm for 473 nm, 532 nm, and 633 nm, respectively. (f) FWHM as a function of laser wavelength, showing an increase with wavelength due to diffraction.

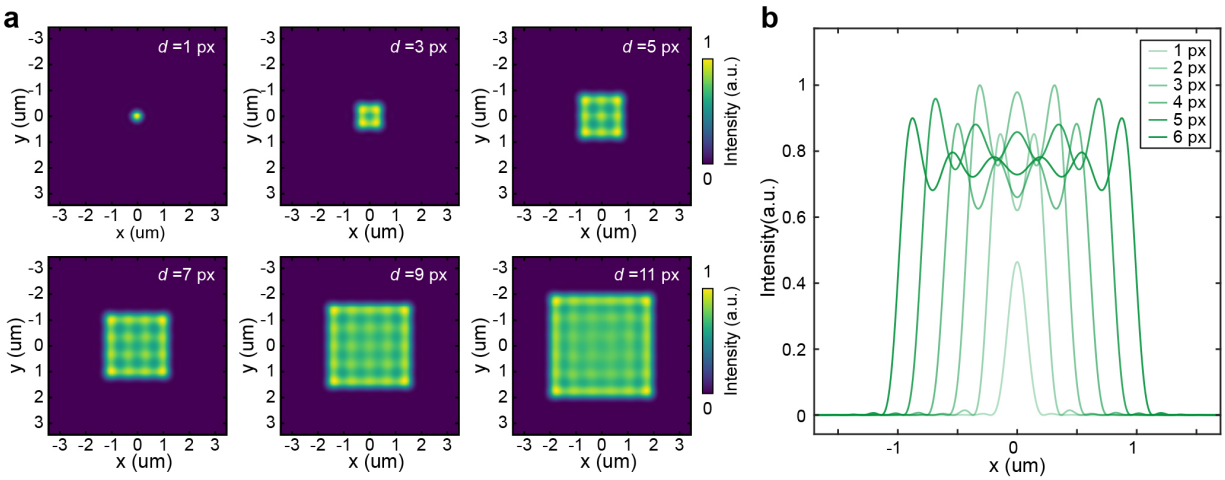

Fig. S9. Simulation of the optical addressing beam using multiple pixels.

(a) Simulated intensity distributions of the optical addressing pattern, where the number of illuminated pixels on the digital mask increases from 1 to 11. (b) Horizontal cross-sectional intensity profiles corresponding to (a), extracted along the centerline of the pattern.

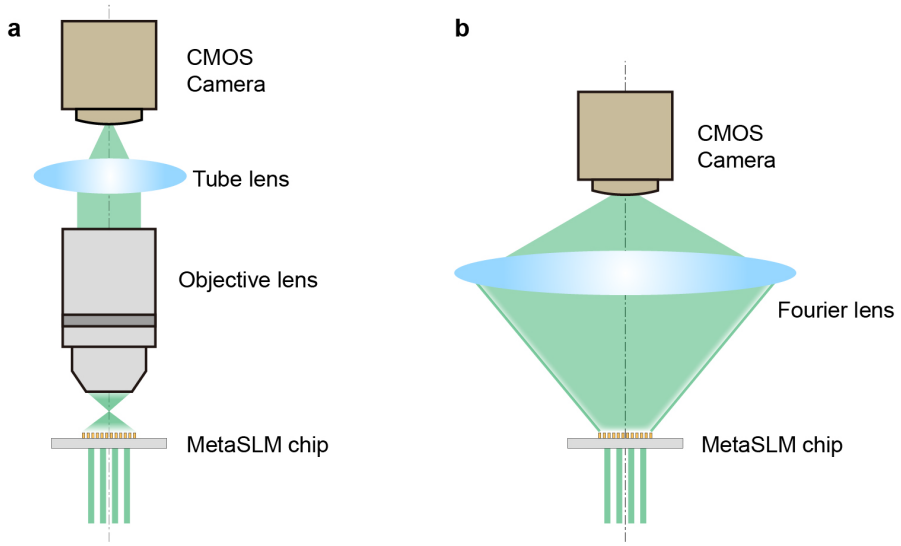

Fig. S10. Schematics of the optical characterization setups.

(a) Experimental setup for focal spot characterization and near-field Fresnel holographic display. The optical addressing pattern is projected onto the metasurface, and the resulting near-field distribution is captured directly by a CMOS camera using a high-NA objective. (b) Setup for capturing the Fourier-transformed holographic patterns. A Fourier lens is placed after the sample to transform the near-field optical field into its far-field Fourier spectrum, enabling holographic reconstruction at the focal plane. The Fourier plane is relayed onto the CMOS camera using a lens system to enable direct imaging of the reconstructed hologram.

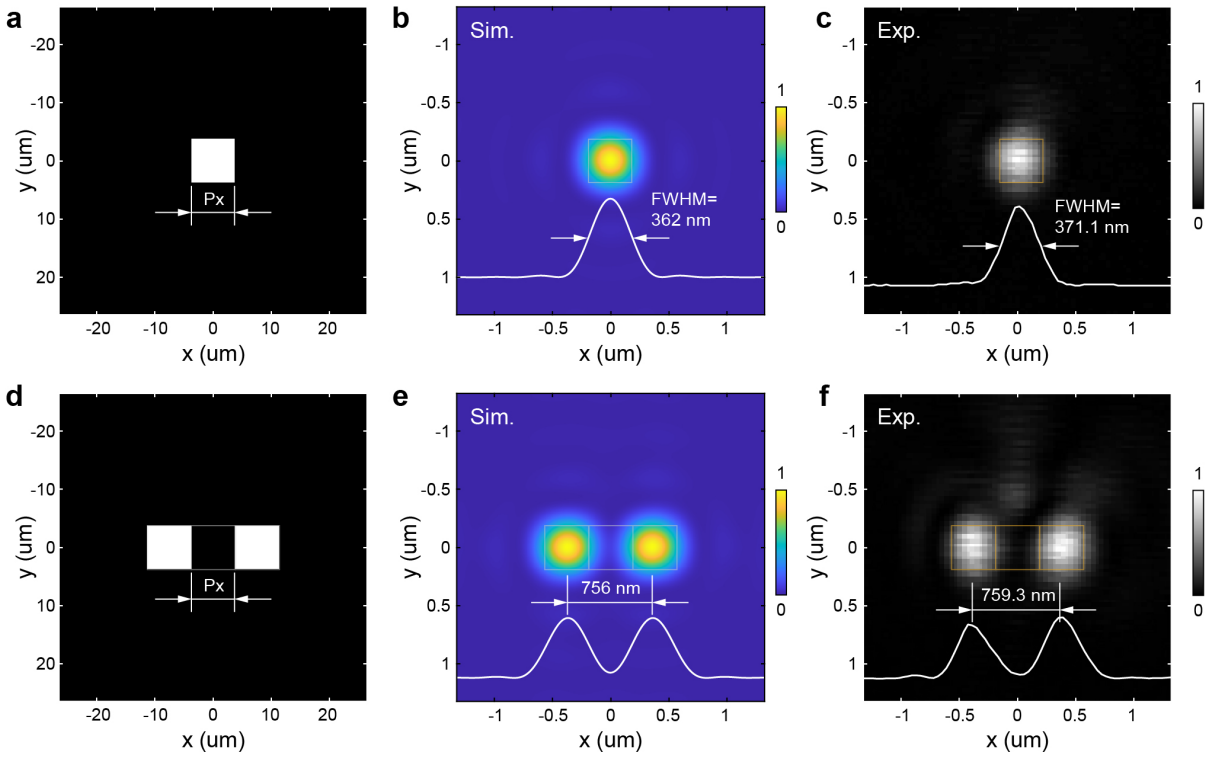

Fig. S11. Experimental characterization of pixel-based optically addressing beam.

(a, d) Pixel-based patterns projected onto the digital mask, with a pixel size of 7.56 μm. Two basic patterns are illustrated: single pixel and interval pixels. (b, e) Simulated intensity profiles (x-y plane) in the focal plane of the optical addressing system for the single-pixel and interval-pixel patterns. (c, f) Experimentally measured intensity profiles (x-y plane) in the focal plane corresponding to the patterns in (a, d).

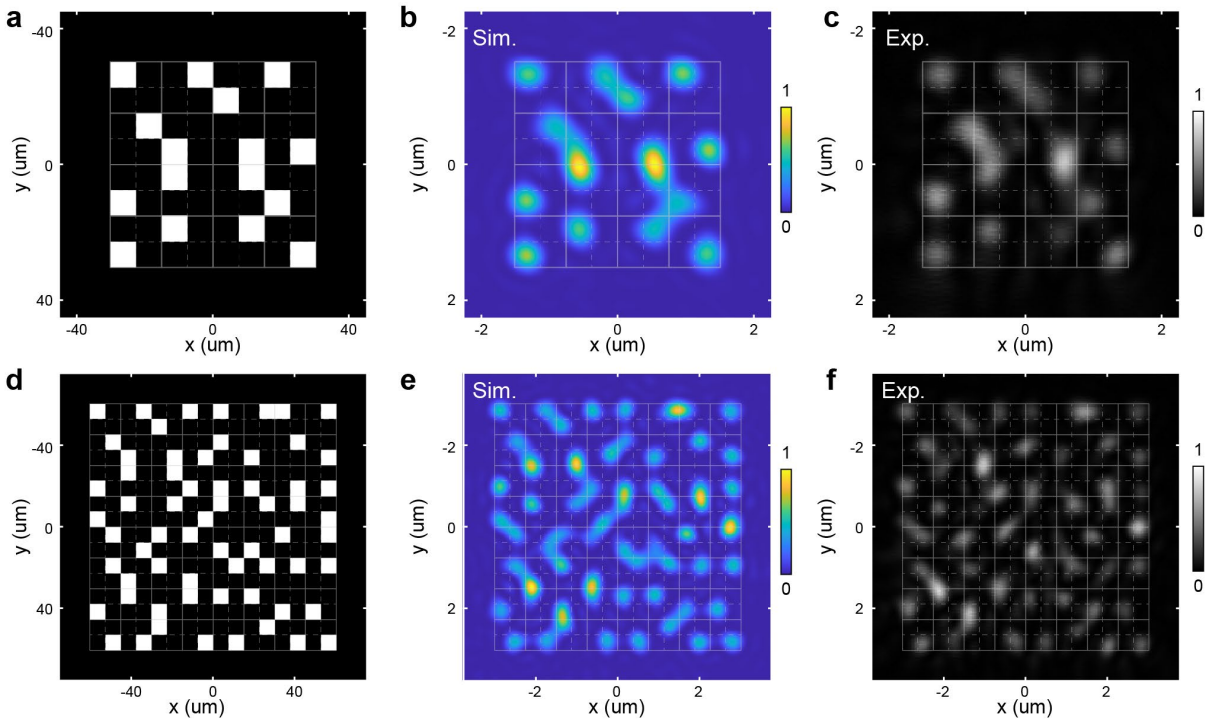

Fig. S12. Demonstration of optical addressing for PDMs composed of 4-level meta-atom supercells.

(a, d) Optical addressing patterns projected onto the digital mask targeting PDMs composed of 4-level meta-atom supercells. The patterns in (a) and (d) correspond to the addressing of 16 and 64 meta-atom supercells, respectively. Each supercell consists of four meta-atoms with pre-discretized phase modulation spanning the full 2π range. The optical addressing beams selectively illuminate one of the four meta-atoms within each supercell according to the designed pattern. (b, e) Simulated intensity profiles (*x*-*y* plane) at the focal plane of the optical addressing system for the patterns shown in (a) and (d). (c, f) Experimentally measured intensity profiles (*x*-*y* plane) at the focal plane corresponding to the patterns in (a) and (d), validating the addressing capability at the meta-atom level.

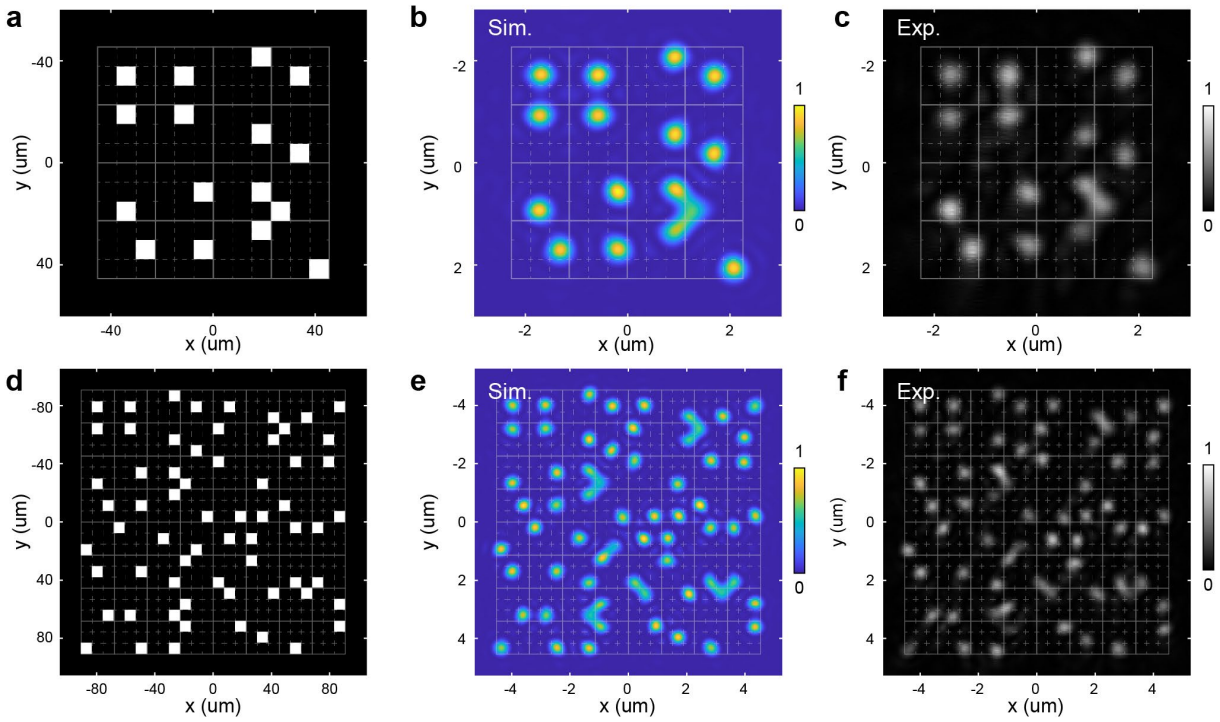

Fig. S13. Demonstration of optical addressing for PDMs composed of 9-level meta-atom supercells.

(a, d) Optical addressing patterns projected onto the digital mask targeting PDMs composed of 9-level meta-atom supercells. The patterns in (a) and (d) correspond to the addressing of 16 and 64 meta-atom supercells, respectively. Each supercell consists of nine meta-atoms with pre-discretized phase modulation spanning the full 2π range. The optical addressing beams selectively illuminate one of the nine meta-atoms within each supercell according to the designed pattern. (b, e) Simulated intensity profiles (*x*-*y* plane) at the focal plane of the optical addressing system for the patterns shown in (a) and (d). (c, f) Experimentally measured intensity profiles (*x*-*y* plane) at the focal plane corresponding to the patterns in (a) and (d), demonstrating high-fidelity addressing performance even for densely packed supercells.

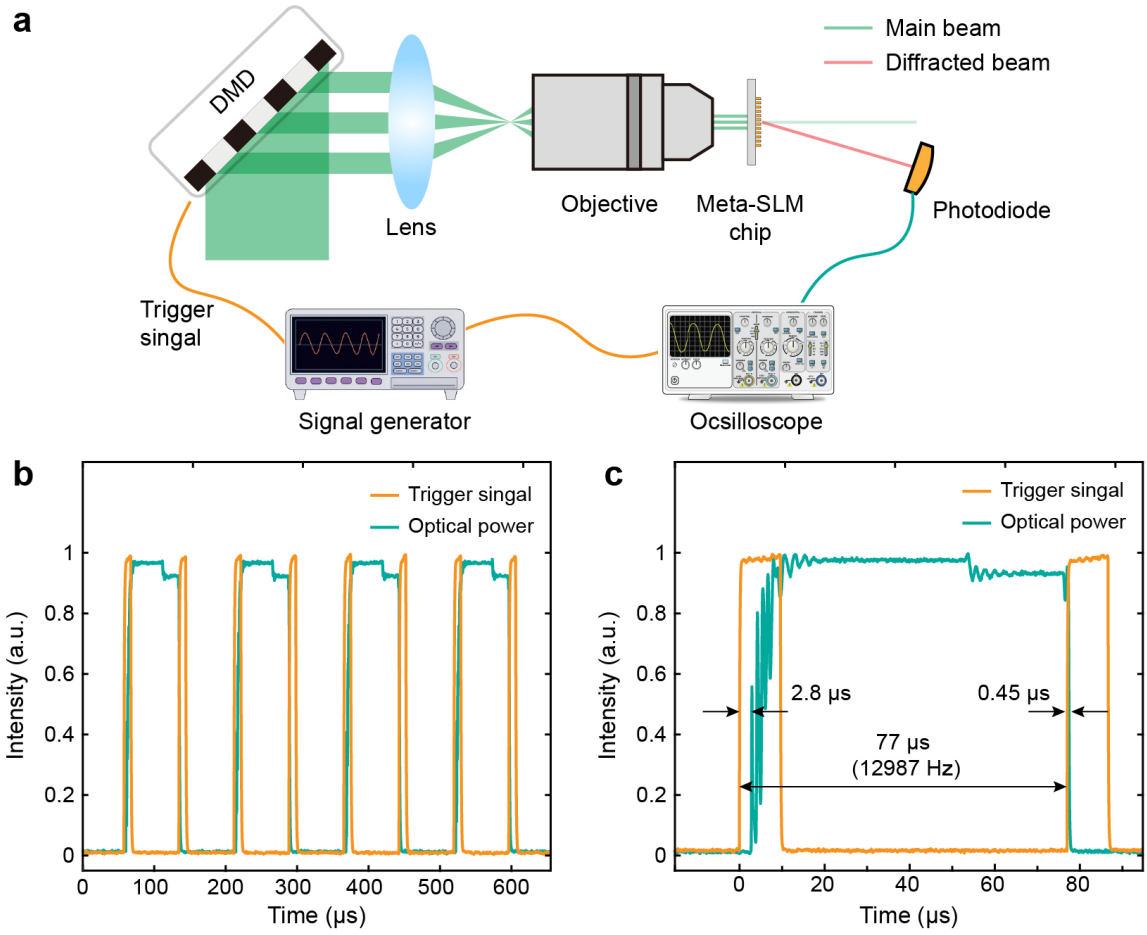

Fig. S14. Experimental characterization of the temporal response.

(a) Schematic of the experimental setup used for temporal response measurement. Voltage signals generated by a signal generator were applied to control the digital mask, producing dynamic optical patterns projected onto the metasurface. The temporal variation of the projected optical field was detected by a high-speed photodiode and recorded by an oscilloscope. (b) Temporal response of the optical addressing system under periodic switching. The yellow curve represents the applied voltage waveform, and the green curve shows the corresponding measured optical power. (c) Temporal response to a single switching event. The measured rise time and fall time of the optical power signal are 2.8 μs and 0.45 μs, respectively. The switching time per frame is 77 μs, corresponding to an operating frequency of 12.987 kHz.

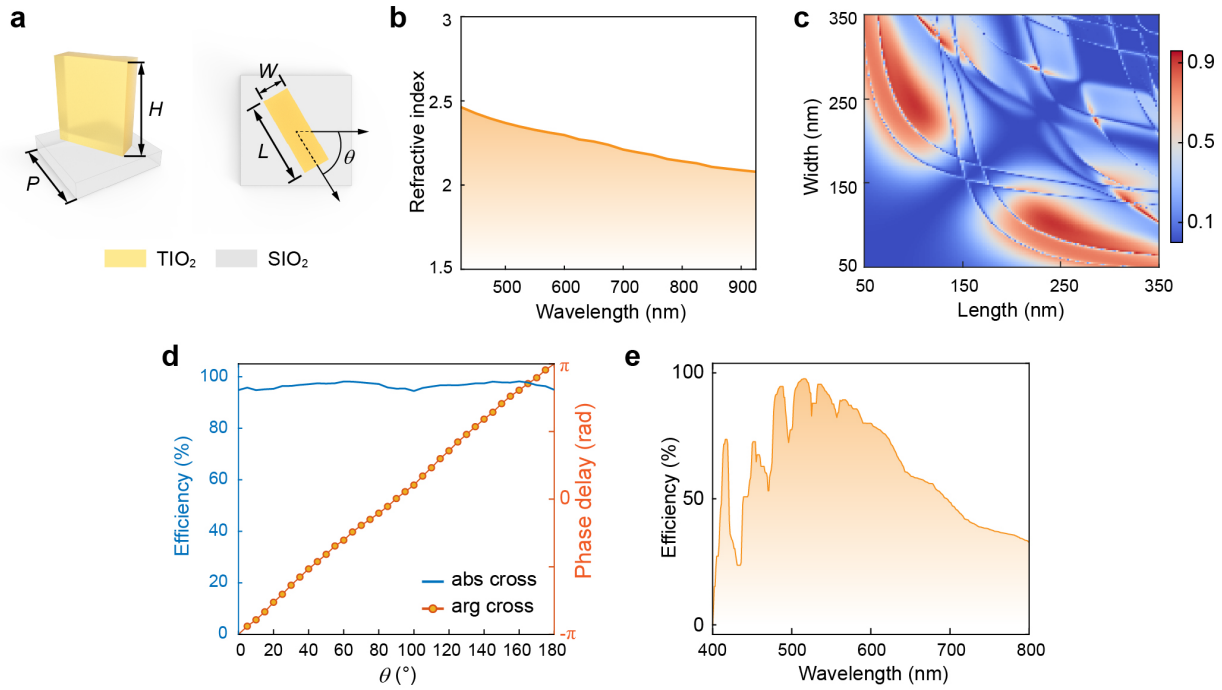

Fig. S15. Electromagnetic responses of the meta-atoms.

(a) Schematic illustration of TiO_2 meta-atoms arranged on a SiO_2 substrate. The parameters L, W, H, P, and θ represent the length, width, height, period, and in-plane rotation angle of each meta-atom, respectively. (b) Refractive index of TiO_2 across the visible spectrum. (c) Numerical simulation of polarization conversion efficiency for meta-atoms with varying lengths and widths under circularly polarized light at a wavelength of 532 nm. The height and period were fixed at 700 nm and 378 nm, respectively. (d) Numerical characterization of conversion efficiency and phase delay for meta-atoms with different orientation angles. (e) Simulated polarization conversion efficiency across the visible spectrum (400–800 nm), showing high performance at the working wavelengths of 473 nm, 532 nm, and 633 nm.

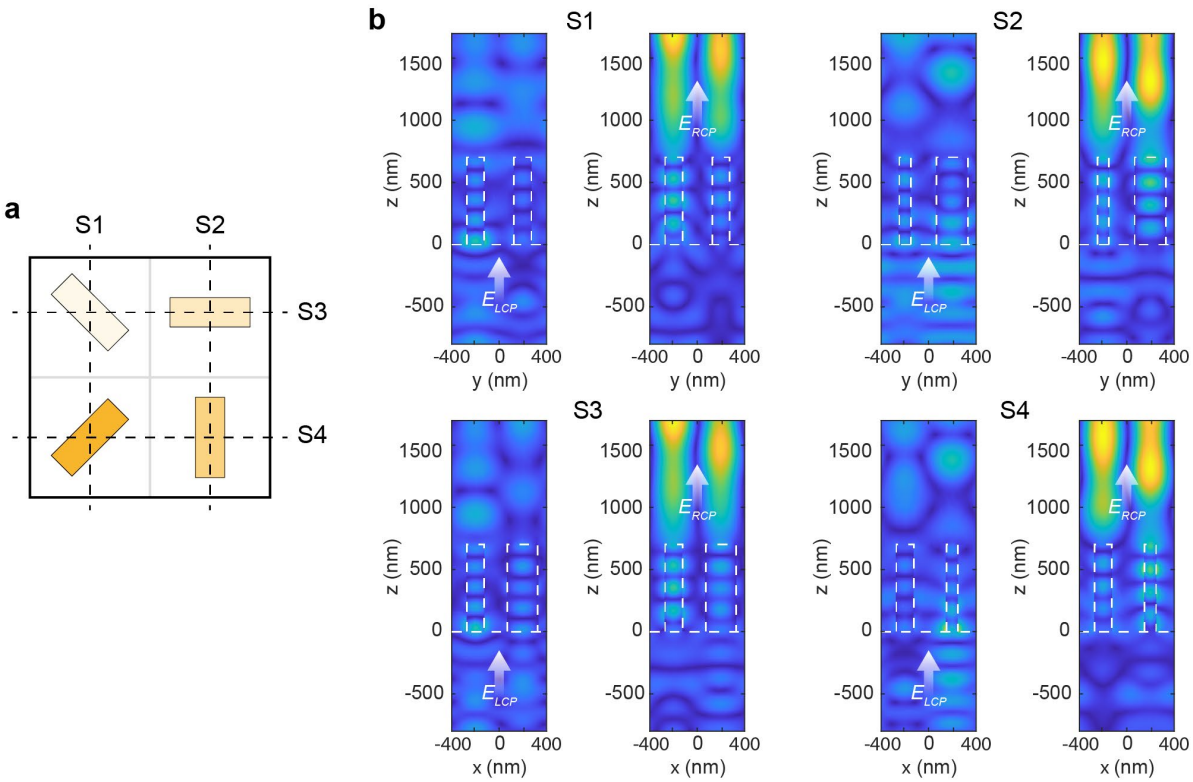

Fig. S16. Electromagnetic response of a meta-atom supercell.

(a) Schematic of a 4-level meta-atom supercell, with simulated cross-sections S1, S2, S3, and S4 indicated by black dashed lines. (b) Simulated electric fields under LCP illumination at the design wavelength of 532 nm, observed along cross-sections S1, S2, S3, and S4, respectively. White arrows indicate the direction of transmitted light, while the dashed boxes mark the positions of the meta-atoms. The electromagnetic response of each meta-atom remains well-confined within its own region, indicating negligible near-field coupling between neighboring meta-atoms. The phase delays agree well with theoretical predictions based on the PB phase, confirming the feasibility of independent phase control at the meta-atom level.

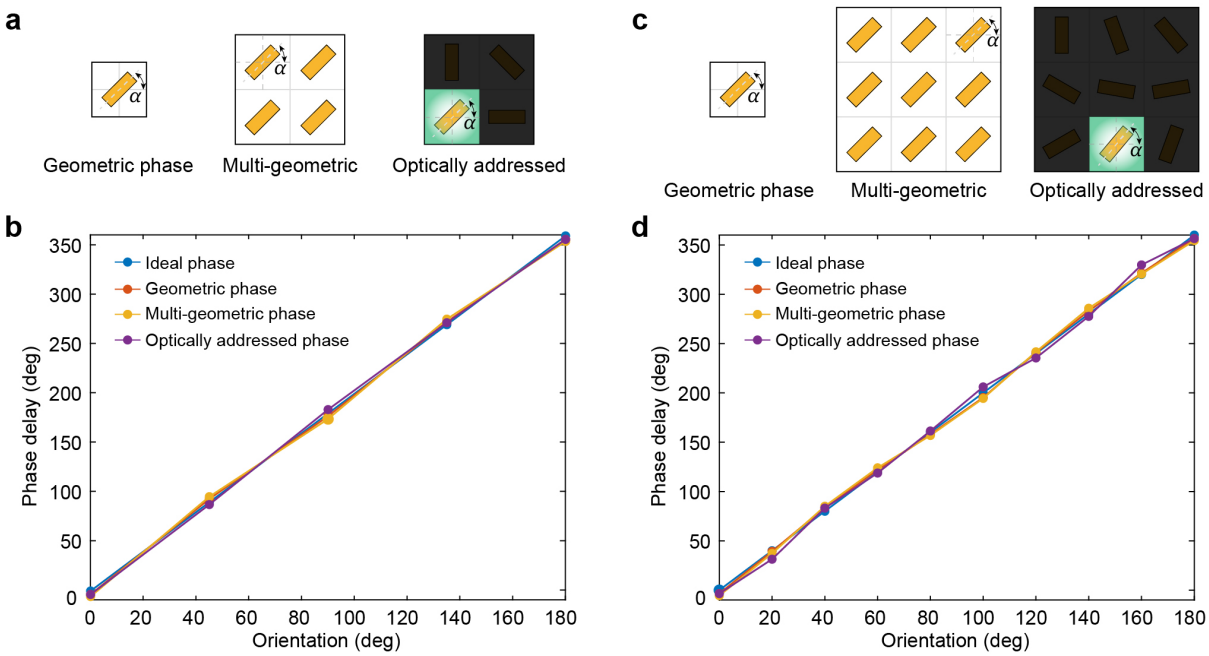

Fig. S17. Impact of phase coupling and phase discretization in meta-atom supercells.

(a) Schematic of different arrangements of meta-atoms: a single geometric meta-atom, multiple geometric meta-atoms, and an optically addressed 4-level meta-atom supercell. (b) Simulated phase delay in the orthogonally polarized light under circular polarization illumination for a 4-level meta-atom supercell. The deviation from the ideal geometric phase is one-twentieth of the designed geometric phase interval, indicating minimal phase coupling. (c) Schematic of different arrangements of meta-atoms: a single geometric unit, multiple geometric units, and an optically addressed 9-level meta-atom supercell. (d) Simulated phase delay in the orthogonally polarized light under CP illumination for a 9-level meta-atom supercell. The deviation from the ideal geometric phase is one-quarter of the designed geometric phase interval, reflecting a higher impact of phase discretization.

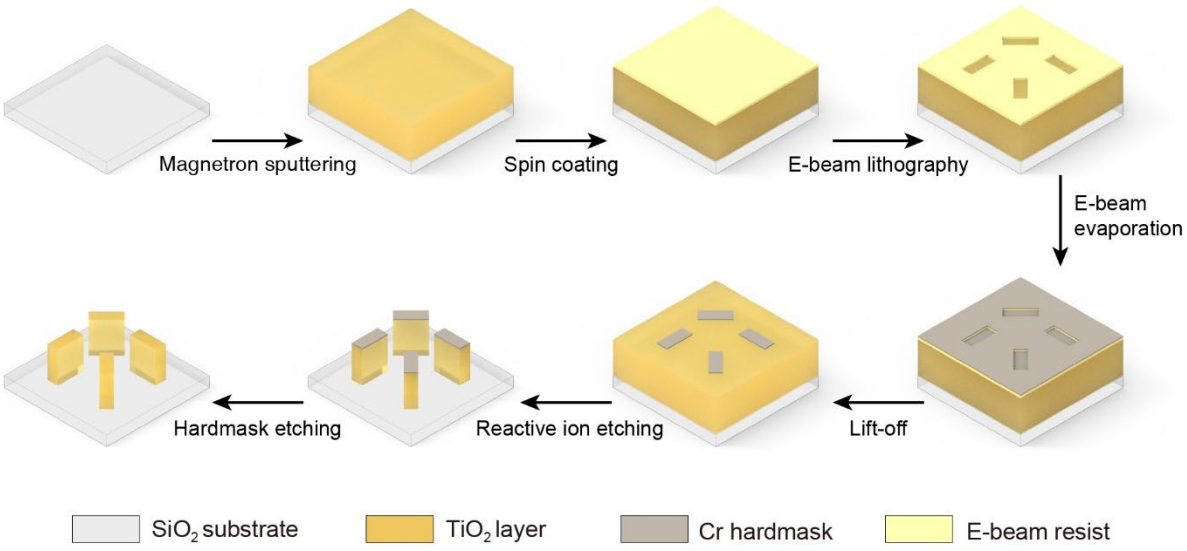

Fig. S18. Schematic of the metasurface fabrication process.

The TiO_2 metasurfaces were fabricated using a combined process of electron beam lithography and reactive ion etching. First, a thin layer of PMMA, approximately 200 nm thick, was spin-coated onto a 700 nm-thick TiO_2 film and patterned by electron-beam lithography. After development in an IPA solution, nanostructures were formed on the resist. A 28 nm-thick Cr layer was then deposited onto the sample using an electron-beam evaporator, followed by a lift-off process to define the hard mask. The TiO_2 film was etched using Cl_2 and C_4F_8 gases in a reactive ion etcher, and finally, the Cr mask was removed, leaving the TiO_2 metasurface nanostructures.

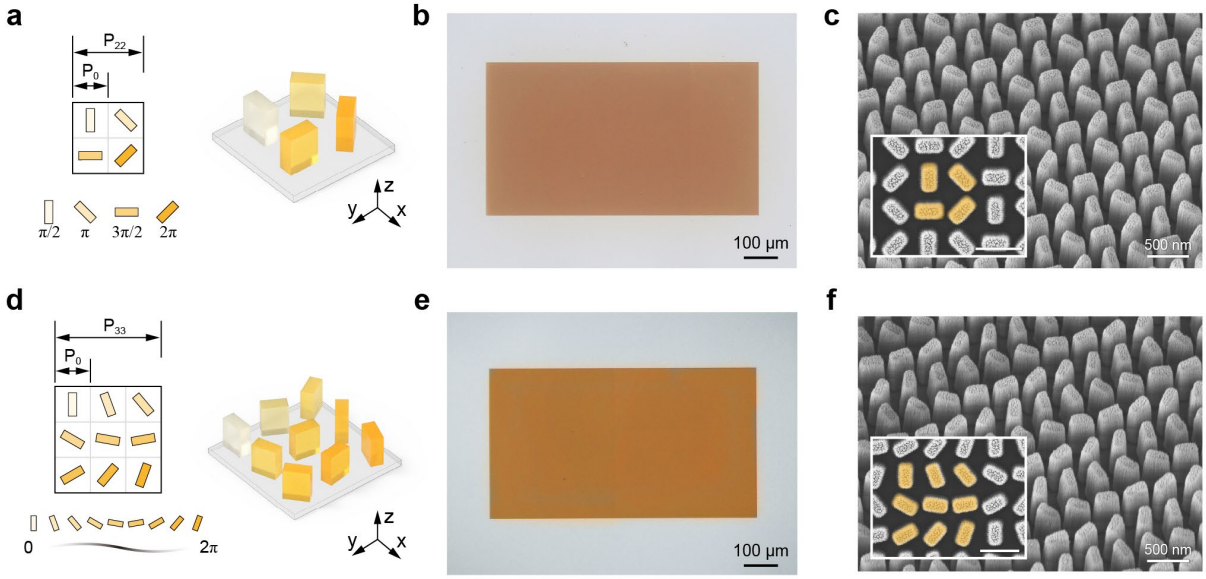

Fig. S19. Fabricated PDMs with arrangements of 4-level and 9-level meta-atom supercells.

(a) Schematic illustration of the arrangement of a 4-level pre-discretized meta-atom supercell, consisting of meta-atoms oriented at -45°, 0°, 45°, and 90°. The period of the meta-atoms is 378 nm, and the period of the meta-atom supercell is 756 nm. (d) Schematic illustration of the arrangement of a 9-level pre-discretized meta-atom supercell consisting of meta-atoms oriented at 20° intervals. The period of the meta-atoms is 378 nm, and the period of the meta-atom supercell is 1134 nm. (b, e) Optical microscope images of the metasurface samples, each with dimensions of 725 μm in length and 408 μm in width. (c, f) SEM images of the metasurface samples, showing the subwavelength, form-birefringent TiO_2 meta-atom supercells comprising the metasurface structures.

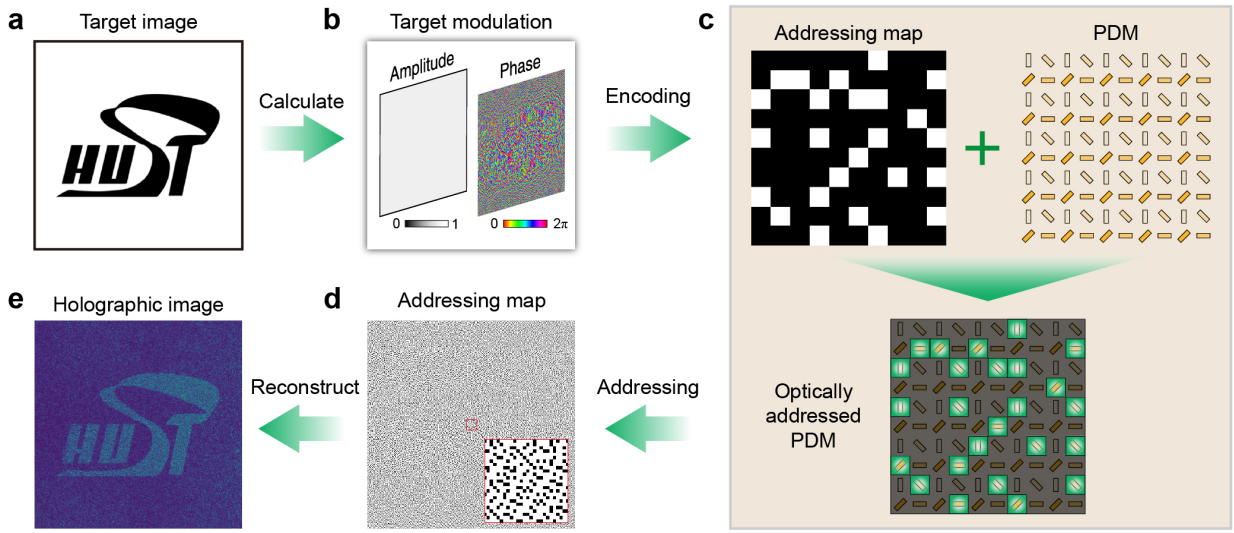

Fig. S20. Workflow for dynamic holographic display using the OA-MSLM.

(a) Target image used for hologram generation, illustrated here with the "HUST" logo. (b) Complex modulation field obtained via holography algorithms. (c) Schematic of the discretization and optical addressing process. The continuous modulation profile is converted into an addressing map, which is combined with a predefined PDM composed of meta-atom supercells to realize dynamic wavefront modulation. (d) Example of an addressing map applied to a 4-level PDM for Fresnel holography. (e) Simulated reconstruction of the holographic image generated by the optically addressed metasurface.

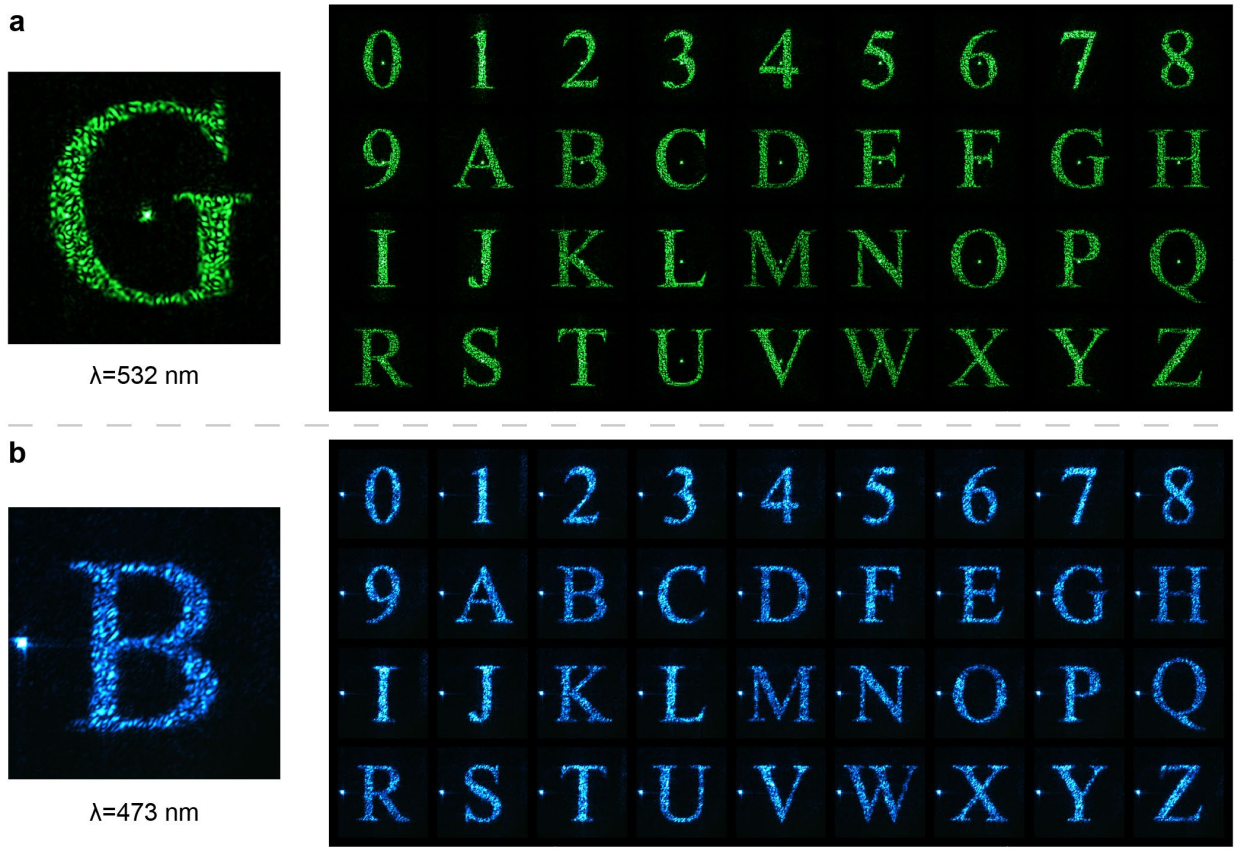

Fig. S21. Experimental demonstration of Fourier holographic display.

(a) Measured on-axis holographic image at the working wavelength of 532 nm. (b) Measured off-axis holographic image at the working wavelength of 473 nm.

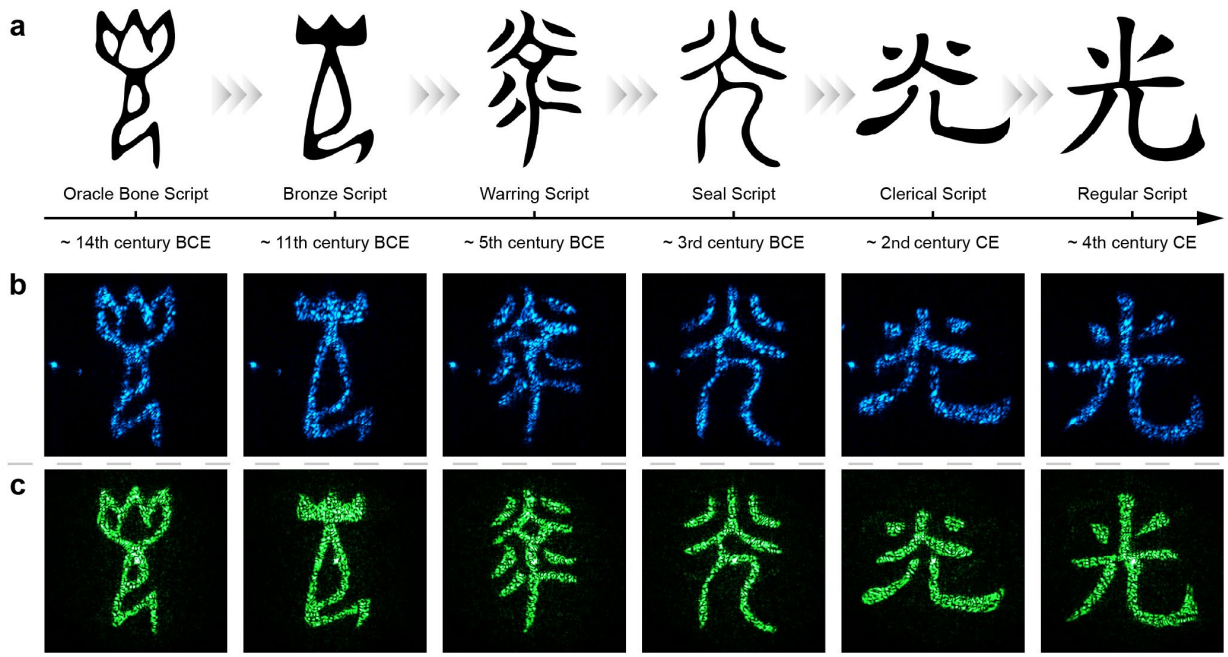

Fig. S22. Dynamic Fourier holographic display of Chinese character evolution.

(a) Target images representing the evolution of the Chinese character "光" (light) from the 14th century BCE to the 4th century CE. Six representative styles were selected for testing the dynamic holographic display. (b, c) Measured raw holographic images at the working wavelength of 473 nm and 532 nm.

Fig. S23. Experimental demonstration of Fresnel holographic display.

(a-c) Measured raw holographic images at the working wavelength of 633 nm, 532 nm, and 473 nm, respectively.

Fig. S24. Dynamic Fresnel holographic display of Chinese character evolution.

(a) Target images illustrating the evolution of the Chinese character "光". (b–d) Measured raw holographic images at 633 nm, 532 nm, and 473 nm, respectively.

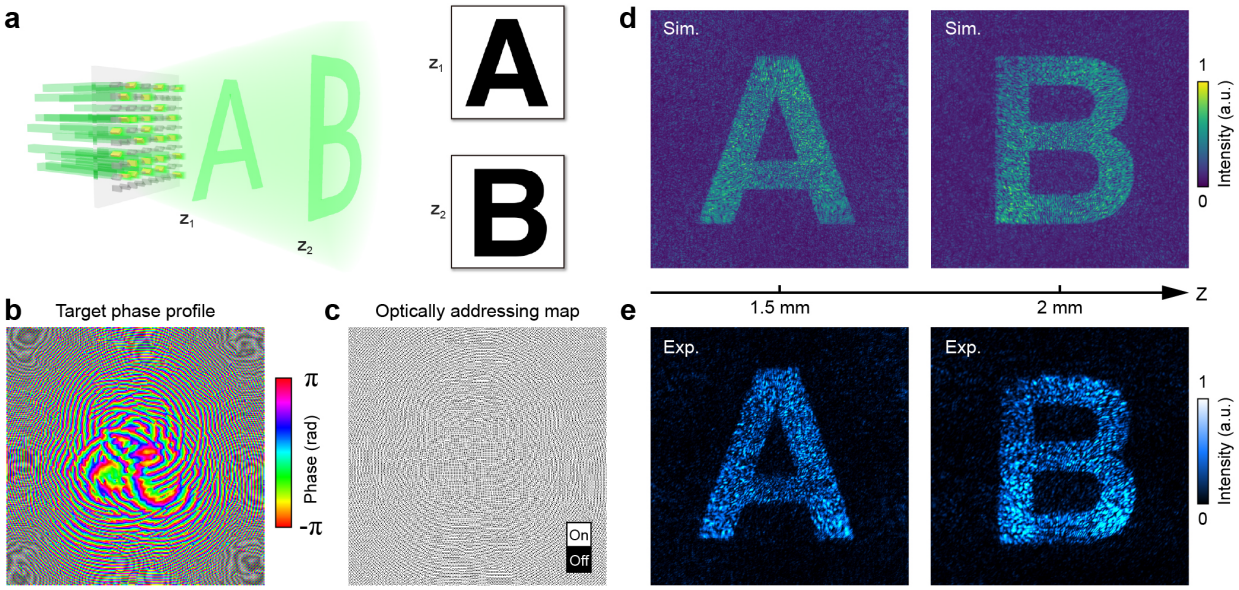

Fig. S25. Demonstration of multi-layer Fresnel holographic display.

(a) Schematic of multi-layer Fresnel holography using an OA-MSLM. (b) Target phase profiles encoded on the OA-MSLM. (c) Optical addressing pattern applied to the metasurface. (d) Simulated reconstructions at 1500 μm and 2000 μm. (e) Experimental reconstructions at 1500 μm and 2000 μm.

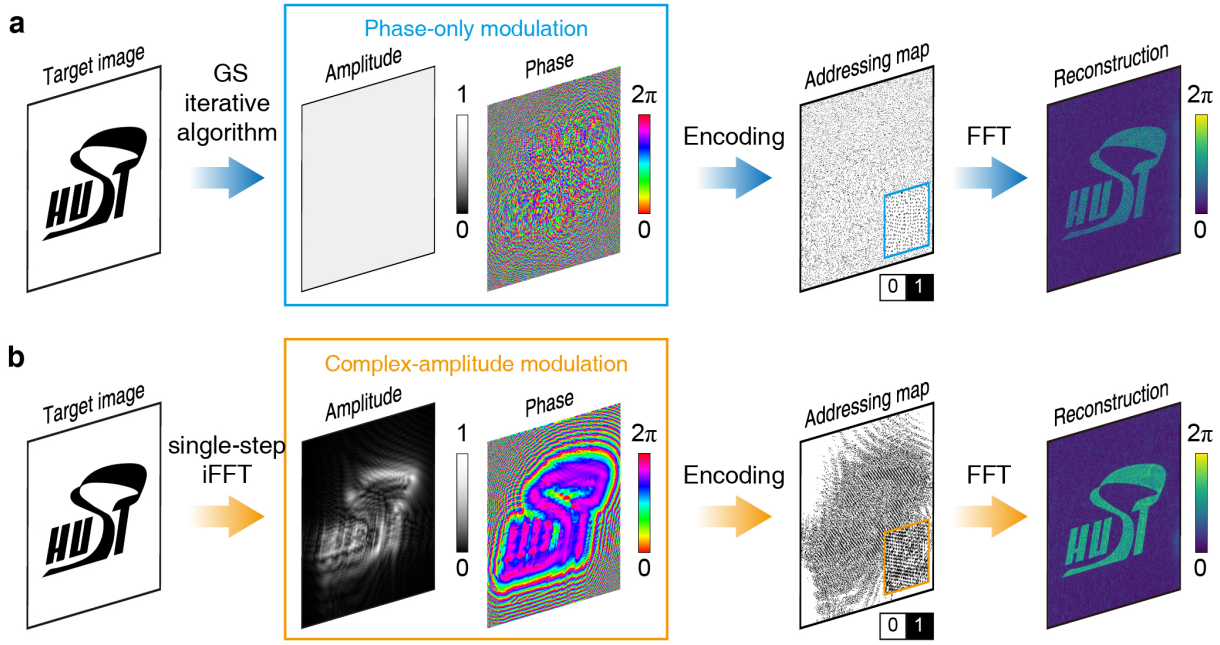

Fig. S26. Comparison between phase-only holography and complex-amplitude holography based on optically addressed OA-MSLM.

(a) Workflow framework for phase-only holography. The target intensity distribution is iteratively reconstructed using the Gerchberg-Saxton algorithm, which optimizes the phase distribution while constraining the amplitude. In the optical addressing pattern, each meta-atom supercell exhibits the same intensity distribution. Dynamic wavefront modulation is achieved through phase modulation introduced by the dynamic optically addressed meta-atom supercells, ultimately producing the desired light field. (b) Workflow framework for complex-amplitude holography. Both phase and amplitude are simultaneously encoded to achieve precise wavefront shaping. The transformed optical addressing pattern drives meta-atom supercells to exhibit distinct amplitude and phase modulation characteristics. The OA-MSLM utilizes pre-designed meta-atom supercell arrangements combined with dynamic optical addressing patterns to enable full control of complex-amplitude, resulting in holographic reconstructions with high fidelity and flexibility.

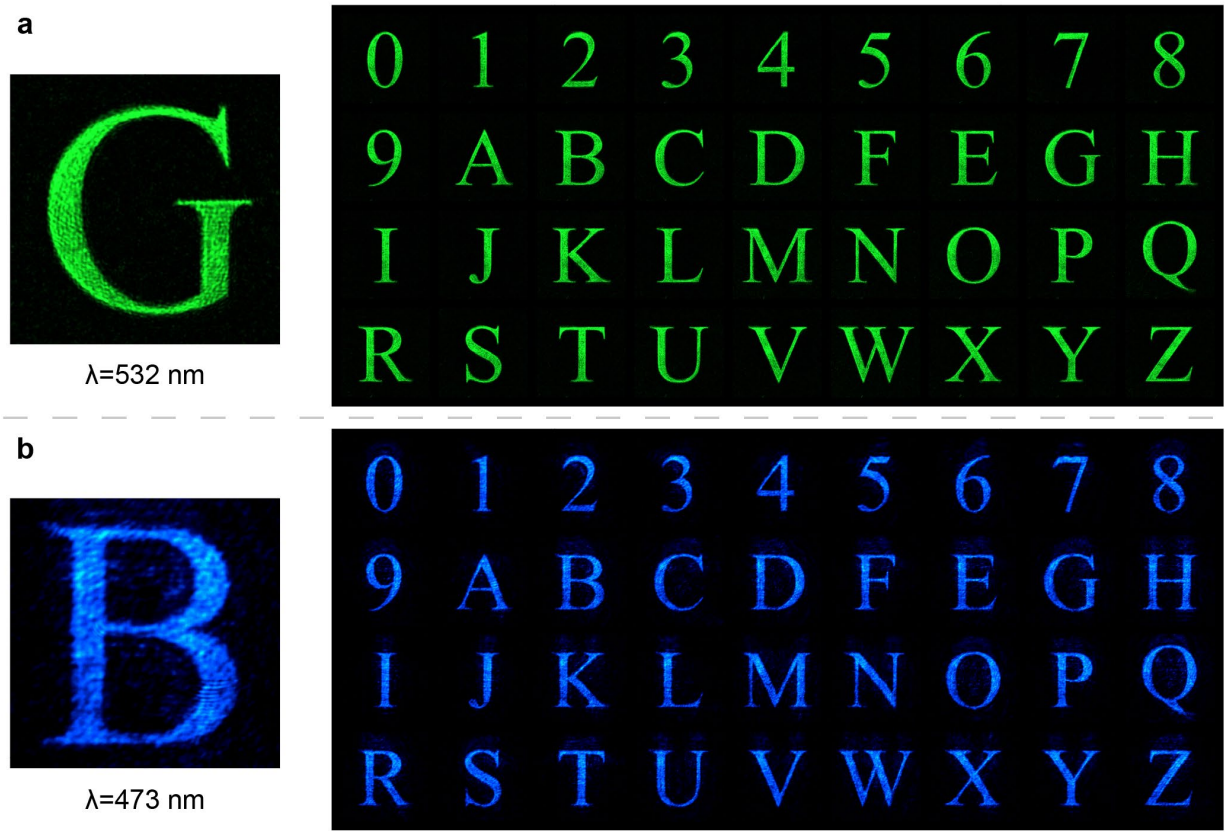

Fig. S27. Experimental demonstration of complex-amplitude holographic display.

(a) Measured raw holographic images at the working wavelength of 532 nm and (b) 473 nm.

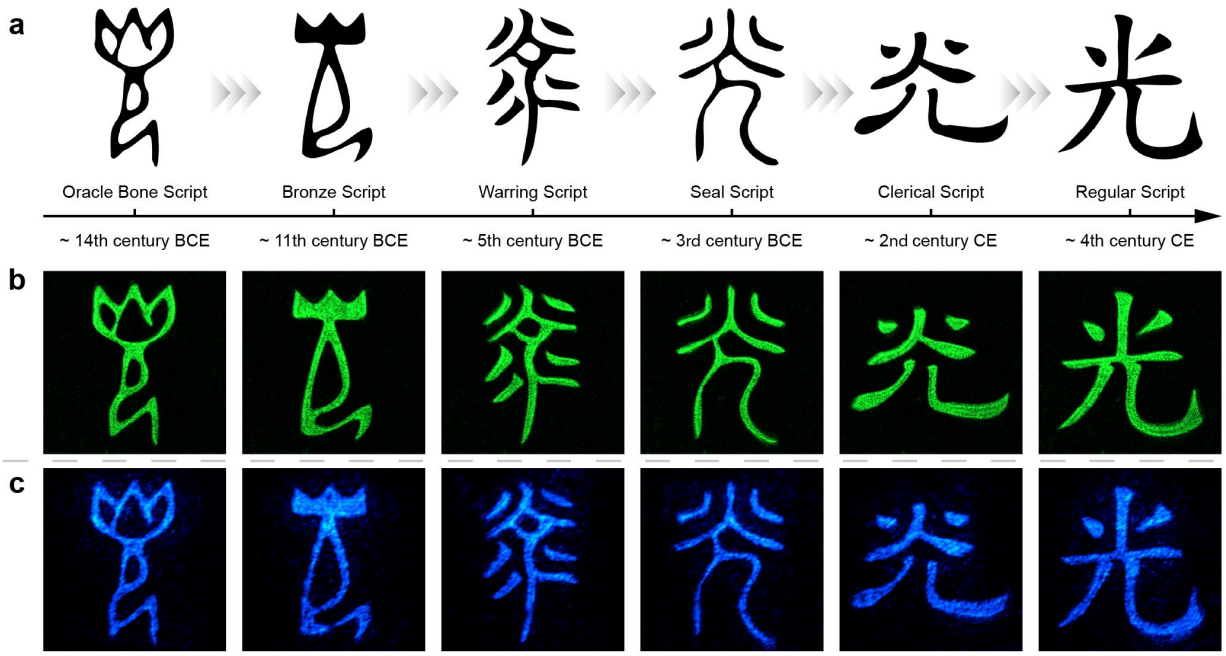

Fig. S28. Complex-amplitude Fresnel holographic display of Chinese character evolution.

(a) Target images illustrating character evolution. (b) Measured images at 532 nm. (c) Measured images at 473 nm.

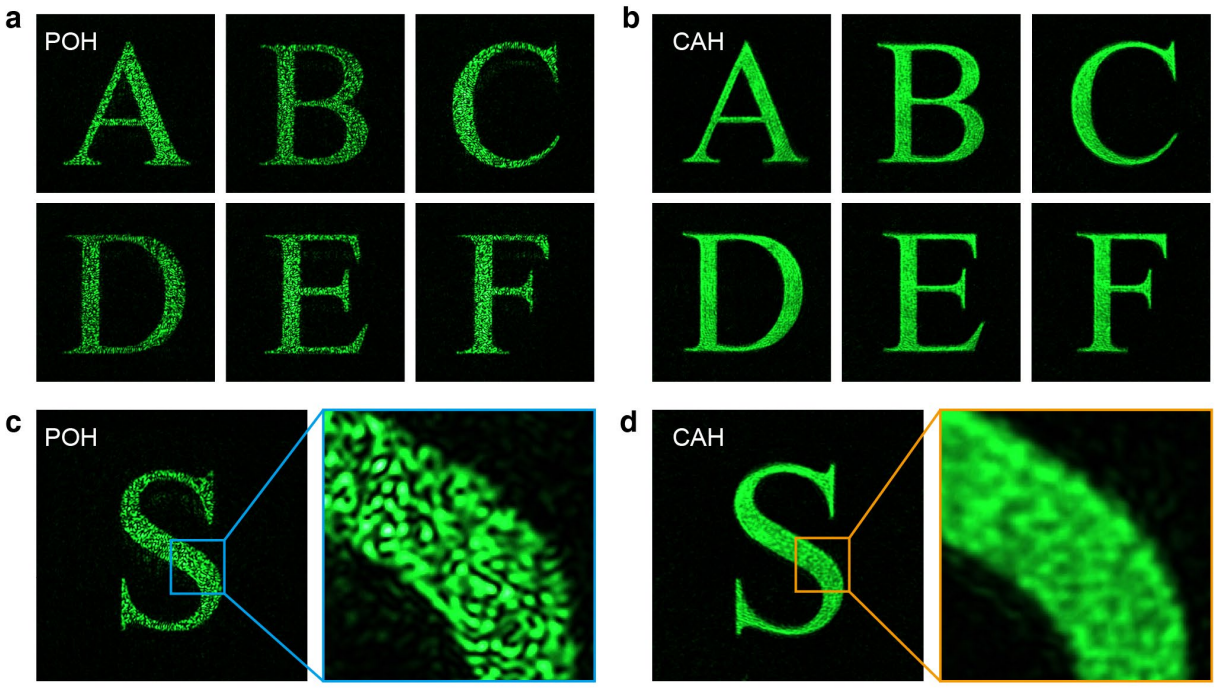

Fig. S29. Experimental comparison between phase-only holography and complex-amplitude holography.

(a, b) Measured raw holographic images generated using phase-only modulation. The working wavelength is 532 nm, and the distance from the metasurface to the holographic focal plane is 1.5 mm. (c, d) Measured and enlarged holographic images of the letter “S” generated using phase-only modulation and complex-amplitude modulation, respectively. The comparison highlights the enhanced fidelity and resolution achieved with complex-amplitude modulation.

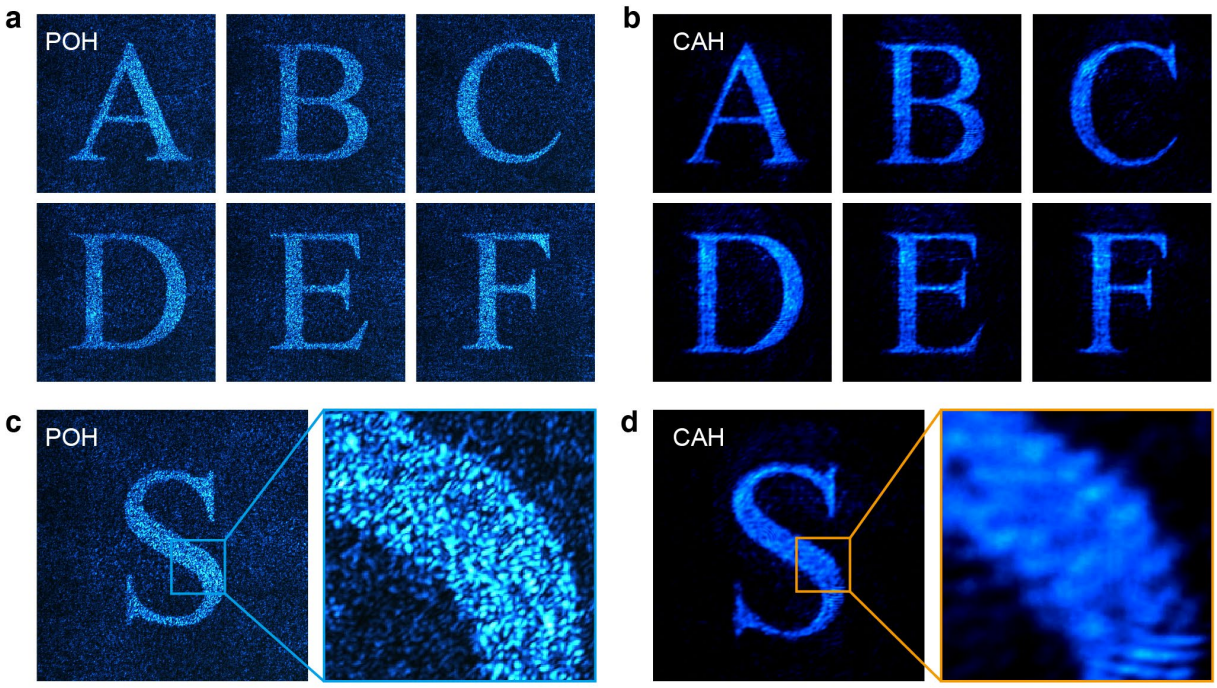

Fig. S30. Experimental comparison between phase-only holography and complex-amplitude holography at the working wavelength of 473 nm.

(a, b) Measured raw holographic images generated using phase-only modulation. The working wavelength is 473 nm, and the distance from the metasurface to the holographic focal plane is 1.5 mm. (c, d) Measured and enlarged holographic images of the letter “S” generated using phase-only modulation and complex-amplitude modulation, respectively. The comparison highlights the enhanced fidelity and resolution achieved with complex-amplitude modulation.

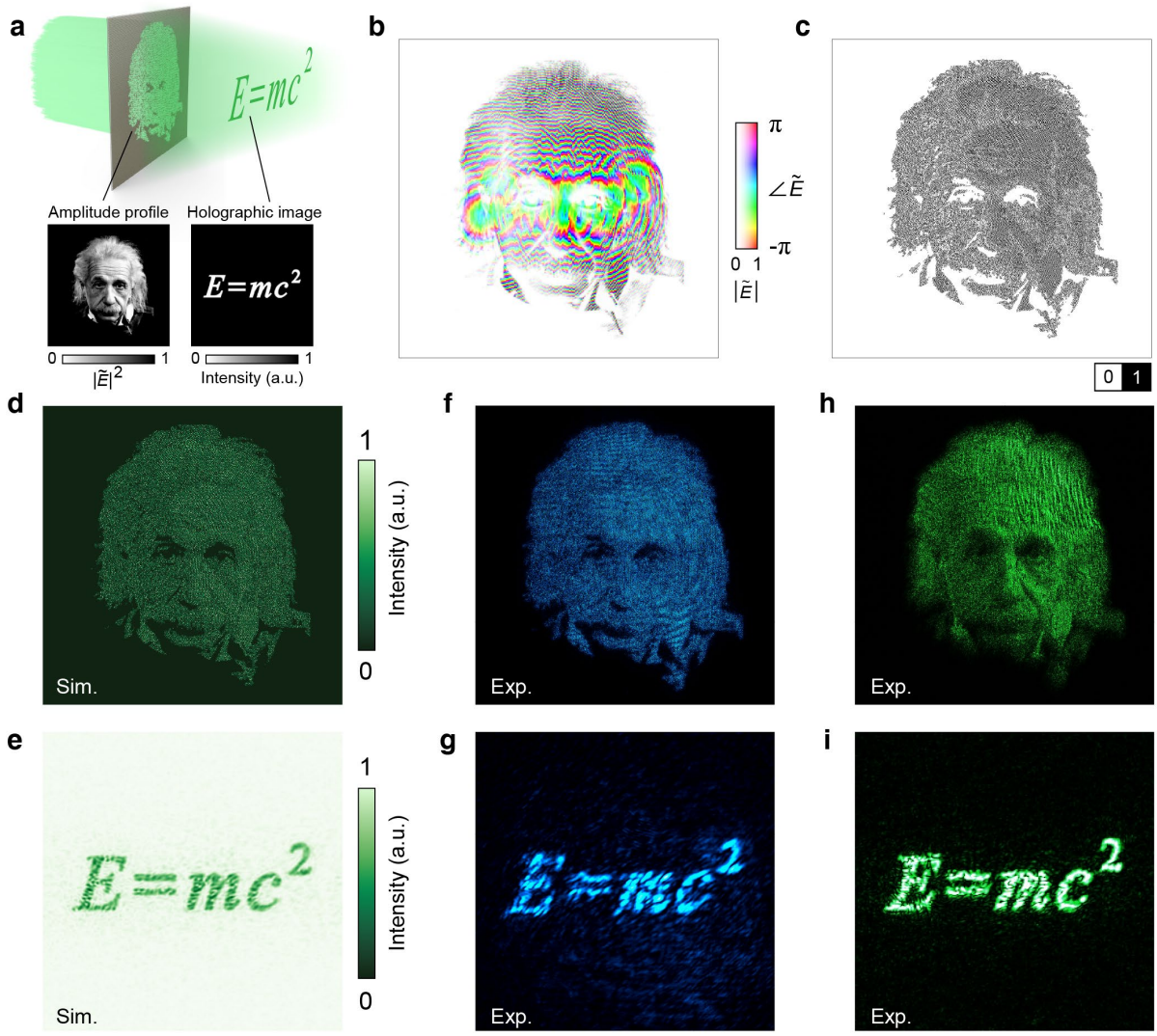

Fig. S31. Double display of an amplitude profile and a Fresnel holographic image.

(a) Schematic illustration of the experimental setup, showing the illumination of a metasurface with an amplitude profile representing a sphere on a flat surface. Two distinct images, "Einstein" and the kinetic energy equation, are encoded using a modified Gerchberg-Saxton algorithm. This encoding enables a grayscale amplitude image at the metasurface plane and a holographic image at the object plane, located 2 mm away. (b) Target intensity and phase profiles encoded on the metasurface for the dual display. (c) An optical addressing pattern was used for illumination on the 9-level PDM. (d, f, h) Simulated and measured reconstructions of the grayscale amplitude profile at the metasurface plane. (e, g, i) Simulated and measured reconstructions of the holographic image at the object plane. The measured reconstructions were collected separately at three distinct working wavelengths: 473 nm and 532 nm.

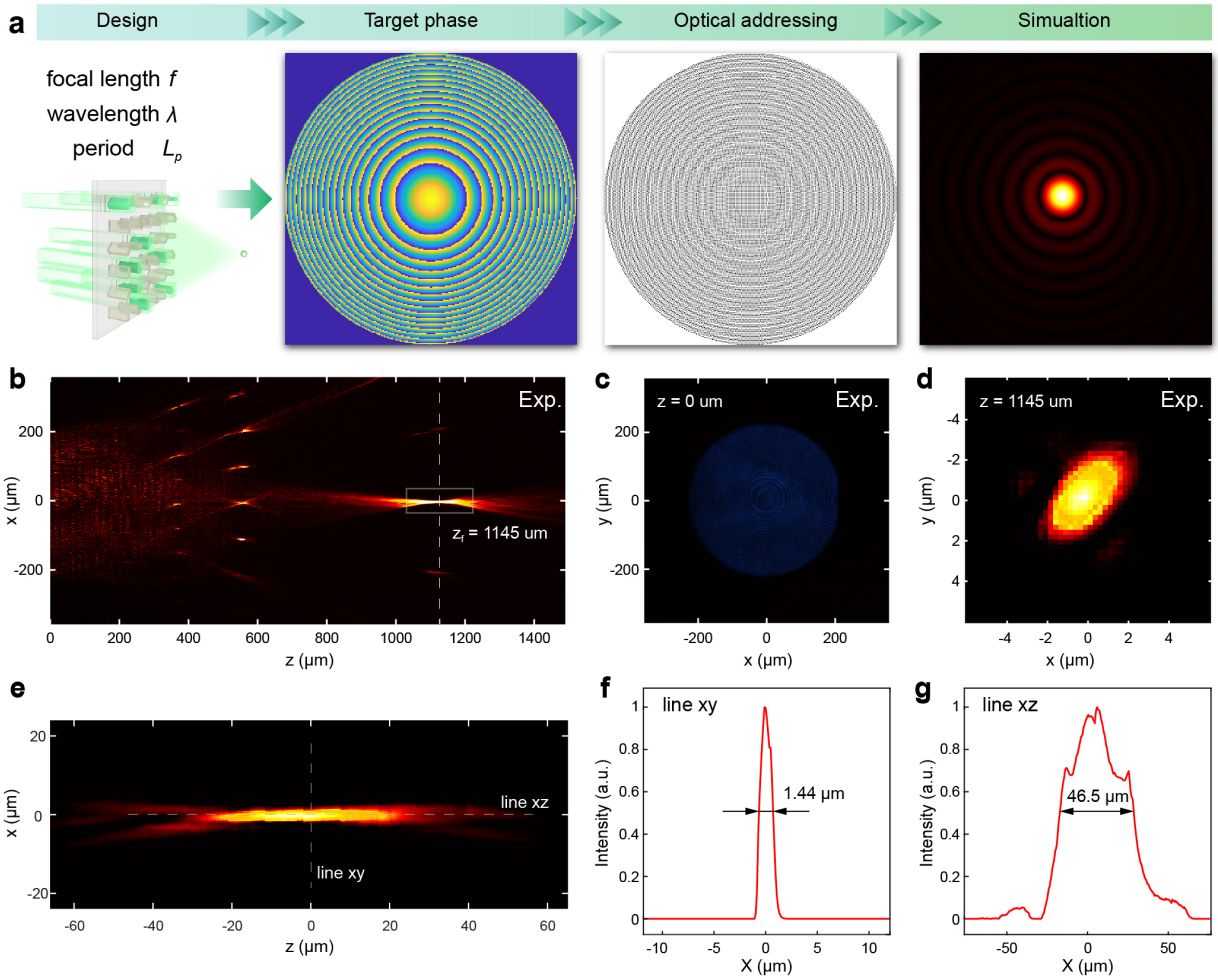

Fig. S32. Demonstration of single focal focusing.

(a) Schematic diagram illustrating the working flow for single focal focusing using an optically addressed OA-MSLM. Target phase profile is generated based on the input parameters, including focal length f, wavelength λ, and pixel period L_p, and is converted into optical addressing beam patterns. (b) Measured intensity distribution along the x-axis as a function of axial distance z, showing beam evolution near the focal plane. (e) Enlarged view of the focal region from (b). (c, d) Measured intensity distributions at the metasurface plane (z = 0 μm) and the focal plane (z = 1145 μm), respectively. (f) Measured intensity profile along the x-axis, passing through the focus. (g) Measured intensity profile along the axis of the lens as a function of distance z around the focus.

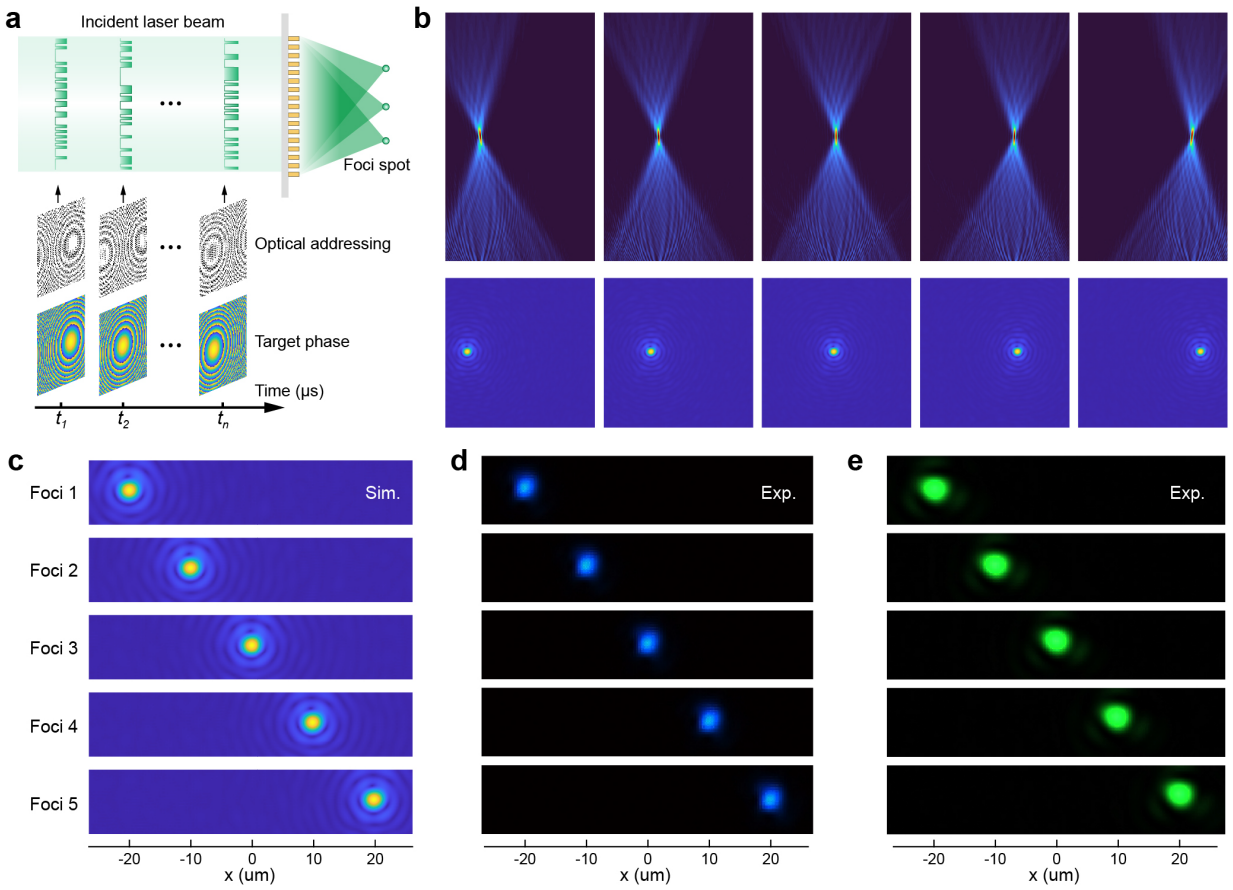

Fig. S33. Demonstration of dynamic planar focal scanning.

(a) Schematic diagram illustrating the generation of dynamic planar focal scanning via temporally loaded optical addressing. Target phase profiles are generated based on the desired focal positions and subsequently converted into optical addressing beam patterns. These beams are sequentially projected onto the pre-discretized metasurface, enabling dynamic scanning of planar focal spots. (b) Simulated intensity distribution of five distinct focal spots, arranged with a designed pitch of 10 μm between adjacent spots, positioned at a focal plane 1.5 mm along the Z-axis. (c) An enlarged view of the simulated x-y plane intensity distribution from (b), showing the detailed intensity profiles of the focal spots. (d, e) Measured intensity distributions at the corresponding focal plane with incident laser wavelengths of 473 nm and 532 nm, respectively.

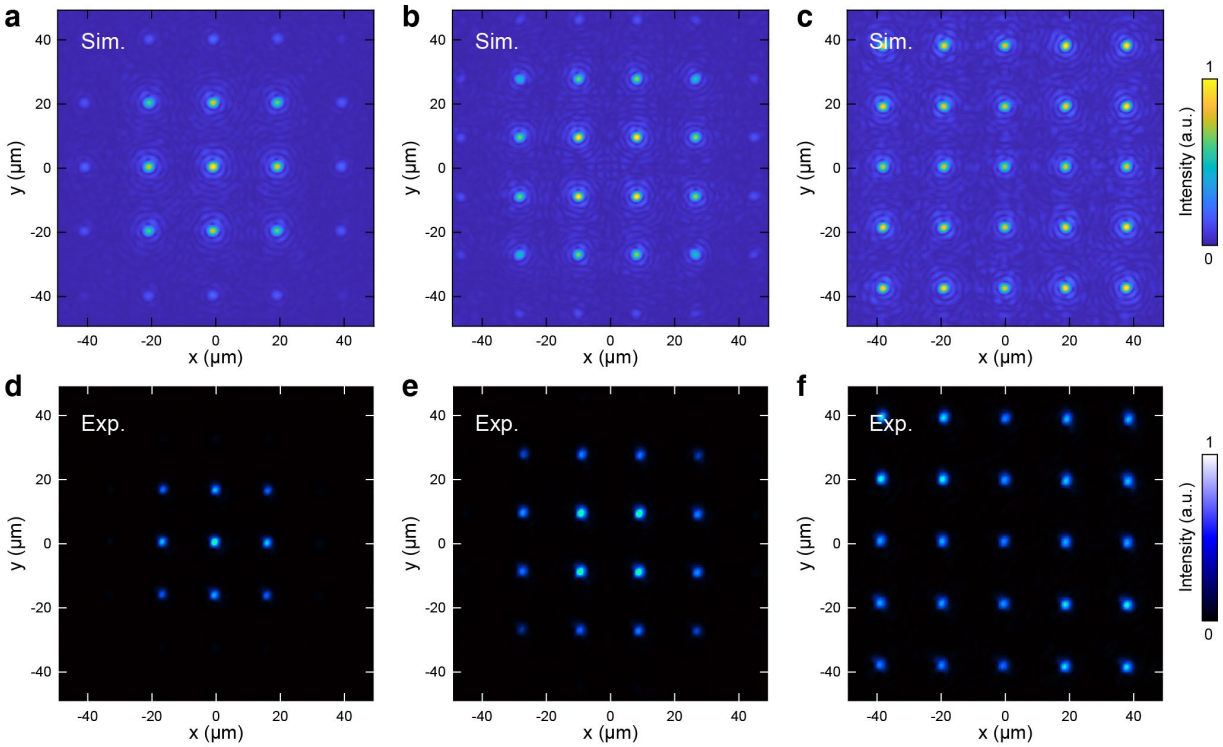

Fig. S34. Demonstration of planar multi-focal spot generation.

(a-c) Simulated multi-focal spot patterns arranged in 3×3, 4×4, and 5×5 grids, respectively, with a designed pitch of 20 μm between adjacent focal spots. The focal plane is positioned at a distance of 1.5 mm along the Z-axis, with a working wavelength of 473 nm. The focal spots are generated by phase profiles encoded on the optical addressing beam and applied to a 4-level pre-discretized metasurface. (d-f) Experimental results of the corresponding multi-focal spot patterns under 473 nm wavelength illumination. The measured patterns closely match the simulated results, demonstrating the accuracy of the metasurface design and its effectiveness in generating planar multi-focal spot arrays.

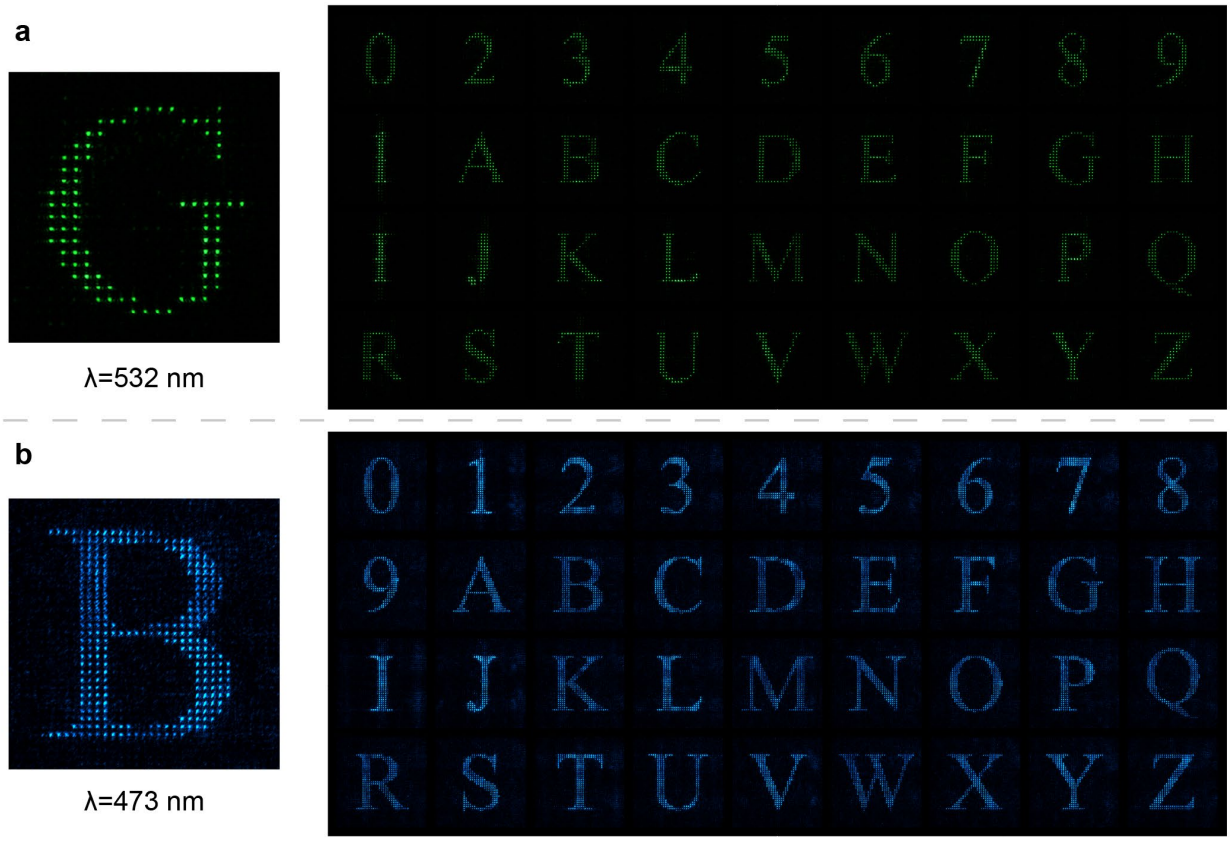

Fig. S35. Experimental demonstration of point-element-based holographic display.

(a) Measured raw holographic images at the working wavelength of 532 nm. (b) Measured raw holographic images at the working wavelength of 473 nm.

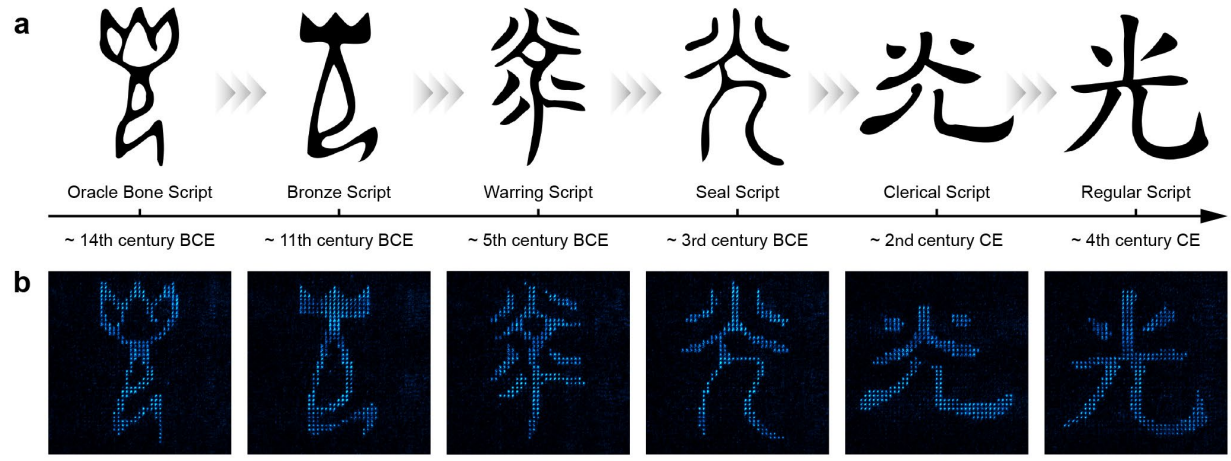

Fig. S36. Point-element-based dynamic holographic display.

(a) Target images illustrating the evolution of the Chinese character "光" (light) from the 14th century BCE to the 4th century CE. Six representative styles were selected to evaluate the performance of the dynamic Fresnel holographic display. (b) Measured raw holographic images at the working wavelength of 473 nm.

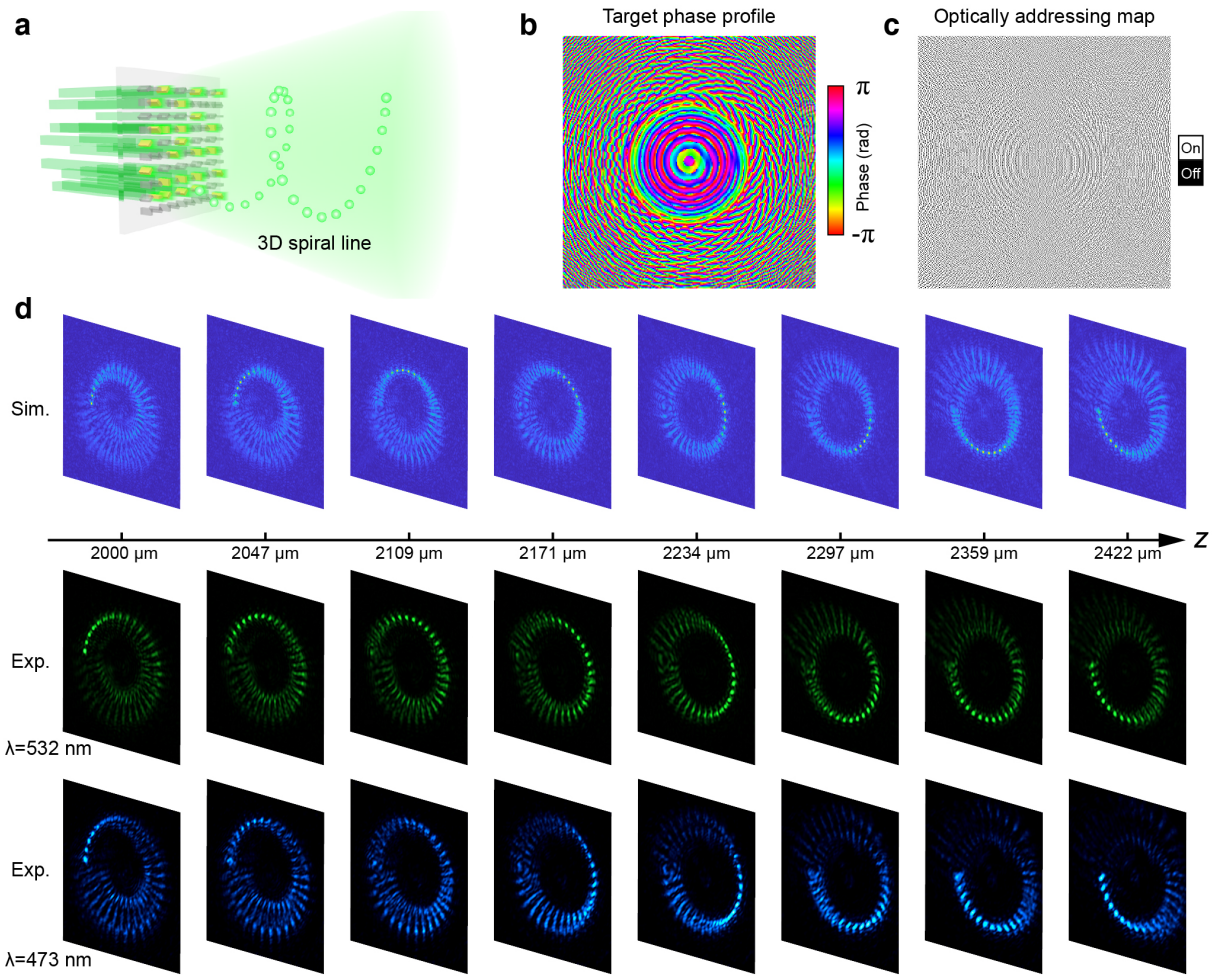

Fig. S37. Demonstration of the generation of 3D focusing along a spiral line.

(a) Schematic illustration of the generation of 3D focusing along a spiral line. The Z-axis represents the axis of the incident addressing beam. (b) Target phase profiles encoded on the OA-MSLM to generate 3D focusing along a spiral line. A total of 32 focal points are designed along the spiral line, which has a radius of 50 μm and a screw pitch of 500 μm. The first focal point is positioned at a distance of 2 mm along the *z*-axis. The working wavelength is set as 532 nm. (c) An optical addressing pattern applied to the 4-level PDM for 3D focusing. (d) Simulated and experimental results show the 3D focusing patterns at various distances. The experimental data were acquired separately at working wavelengths of 473 nm and 532 nm.

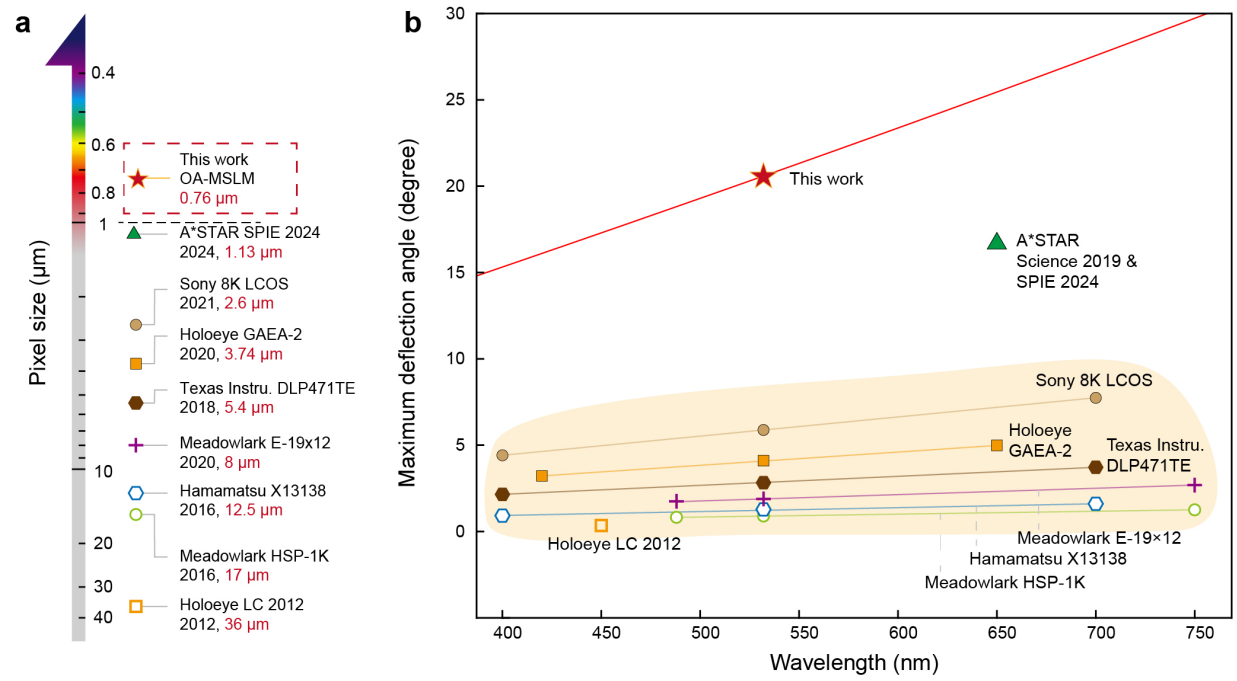

Fig. S38. Comparison of pixel size and maximum deflection angle across different 2D beam deflection approaches.

(a) Pixel sizes of various 2D beam deflection approaches, represented by different symbols. References for all data points are provided in Supplementary Table S2. (b) Maximum deflection angles achieved by different beam deflection approaches, plotted as a function of the working wavelength (horizontal axis) and maximum deflection angle (left vertical axis). Theoretical maximum deflection angles for the present work are represented by a red curve, while the experimentally measured result at 532 nm is indicated by a red star symbol. Data for conventional SLMs are highlighted with a yellow background.

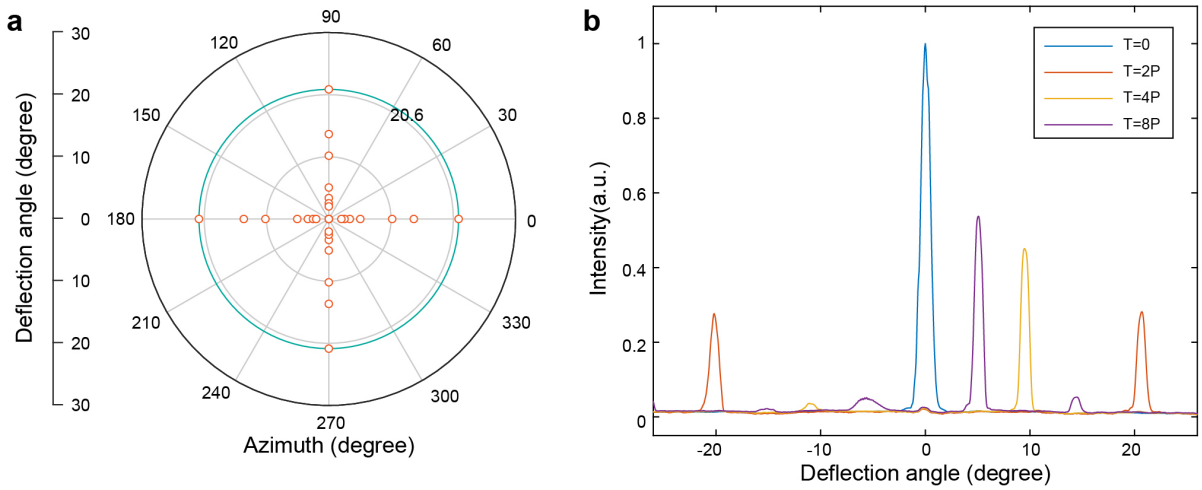

Fig. S39. Characterization of beam deflection performance.

(a) Calculated angular distribution of the deflected beam. Scatter points represent the results obtained after modulo-addition of all possible coding sequences along the x- and z-axes of the OA-MSLM. (b) Measured angular distribution of the deflected beam for different grating periods.

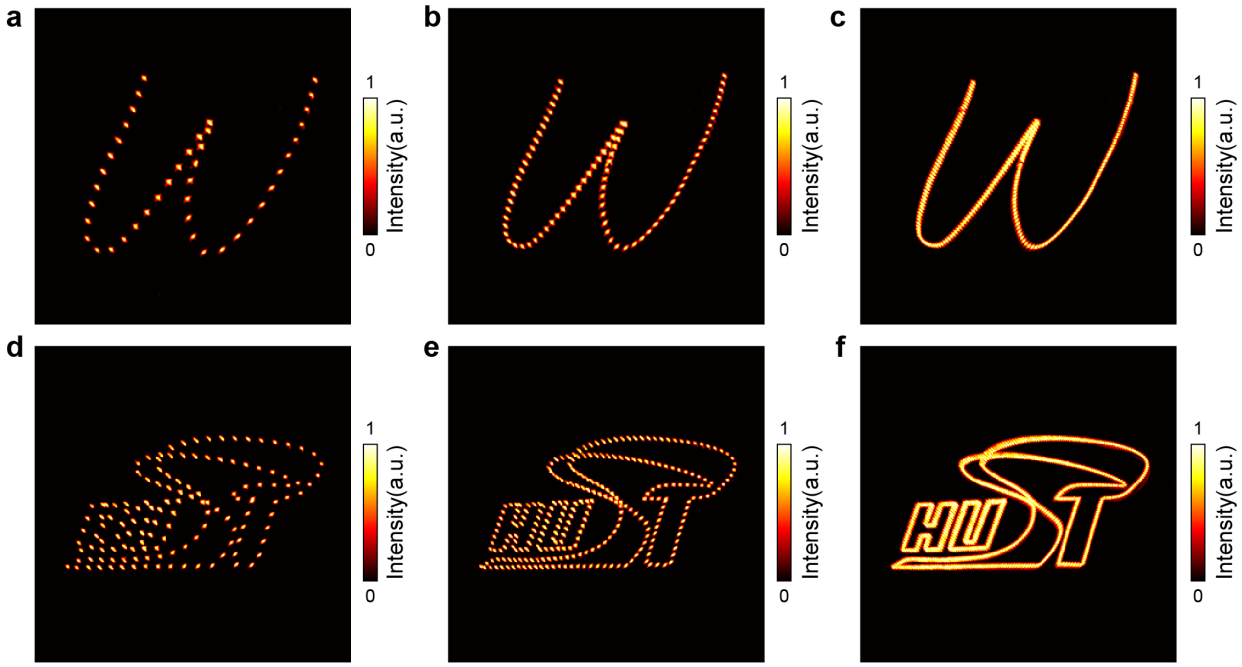

Fig. S40. Demonstration of 2D patterned beam deflection.

(a–c) Experimentally measured beam deflection patterns corresponding to a scanned handwritten "W" pattern with 42, 84, and 209 distinct output beam directions, respectively. (d–f) Experimentally measured beam deflection patterns corresponding to a scanned "HUST" logo pattern with 135, 268, and 668 distinct output beam directions, respectively. Each scanned pattern was reconstructed by stacking the maximum intensity values from independently recorded intensity distributions at each scan step.

Supplementary Tables

Supplementary Table S1 Source data corresponding to Fig. 1A.

Device model	Type	Dimensionality	Pixel Pitch (μm)	Pixel number (pixels)	Refresh rate (Hz)	SPTD (pixels/(s • cm²))
Holoeye LC2012 2012 [9]	Transmissive LCOS	2D	36	1024 × 768	60 Hz	4.6×10^{6}
Meadowlark HSP-1k 2016 [10]	Reflective LCOS	2D	17	1024 × 1024	1400 Hz	4.8×10^{8}
Hamamatsu X13138 2016 [11]	Reflective LCOS	2D	12.5	1272 × 1024	60 Hz	3.8×10^{7}
Meadowlark E-19x12 2020 [12]	Reflective LCOS	2D	8	1920 × 1200	1350 Hz	2.1×10^{9}
Texas Instruments DLP472TE 2018 [13]	DMD	2D	5.4	1920 × 1080	60 Hz	2.1×10^{8}
Holoeye GAEA-2 2020 [14]	Reflective LCOS	2D	3.74	4160 × 2464	180 Hz	1.3×10^{9}
Sony 8K LCOS 2021 [15]	Reflective LCOS	2D	2.6	7680 × 4320	120 Hz	1.8×10^{9}
Caltech Nano Letter 2016[16]	ITO-based	1D	1.6	1 × 48	10 MHz	6.3×10^{10}
Caltech ACS Nano 2020[17]	ITO-based	1D	0.504	1 × 96	1 MHz	2.0×10^{10}
Samsung Nat. Nano. 2021[8]	ITO-based	1D	5	1 × 100	5.4 MHz	1.1×10^{10}
Caltech Nat. Nano. 2024[18]	ITO-based	1D	5	1 × 20	1 MHz	2.0×10^{9}
UWashington ACS Nano 2024[19]	PCM-based	1D	1.8	1 × 17	20 kHz	1.1×10^{8}
Harvard Nat. Comm. 2021[20]	EOM-based	1D	0.9	1 × 20	100 kHz	1.1×10^{9}
A*STAR Science 2019[21]	LC+Metasurface	1D	1.14	1 × 28	1 kHz	8.8×10^{6}
A*STAR Light Sci. Appl. 2022[22]	LC+DBR	1D	1.14	1 × 96	1 kHz	8.8×10^{6}
A*STAR ACS Nano 2023[23]	LC+Metasurface	1D	1.14	1 × 96	10 kHz	8.8×10^{7}
A*STAR SPIE 2024[24]	LC+Metasurface	2D	1.14	640 × 480	1 kHz	7.7×10^{10}
HUST This work OA-MSLM 2025	**Optical addressing**	**2D**	**0.756**	**960 × 540**	**13 kHz**	$\mathbf{2.3\times10^{12}}$

Supplementary Table S2. Comparison of the proposed optically addressed OA-MSLM and existing 2D SLMs in terms of the pixel size and maximum deflection angle.

Type	Device model/ Ref.	Pixel Pitch (μm)	Wavelength (nm)	Deflection angle (°)
LCOS	Sony 8K LCOS[15]	2.6	400	4.41
			532	5.87
			700	7.74
LCOS	Holoeye GAEA-2[14]	3.74	420	3.22
			532	4.08
			650	4.99
DMD	Texas Instruments DLP471TE[13]	5.4	400	2.12
			532	2.82
			700	3.72
LCOS	Meadowlark E-19×12[12]	8	488	1.75
			532	1.91
			633	2.27
LCOS	Hamamatsu X13138[11]	12.5	400	0.92
			532	1.22
			700	1.60
LCOS	Meadowlark HSP-1K[10]	17	488	0.82
			532	0.90
			750	1.26
LCOS	Holoeye LC 2012[9]	36	450	0.36
LC + Meta	Science 2019, 364 (6445), 1087–1090 (1D)[21] High Contrast Metastructures XIII SPIE 2024 (2D)[24]	1.14	650	10.96
Optical addressing	**This work**	**0.756**	**472**	**18.19**
			532	**20.60**
			633	**24.75**

Captions for Supplementary Movies

Movie S1. Far-field Fourier holographic display.
Demonstration of a far-field dynamic holographic display reconstructed using Fourier holography.

Movie S2. Near-field Fresnel holographic display.
Demonstration of a near-field dynamic holographic display reconstructed using Fresnel diffraction.

Movie S3. Multi-layer Fresnel holographic display.
Demonstration of multi-layer Fresnel holographic reconstruction with focal planes positioned along the z-axis.

Movie S4. Complex-amplitude Fresnel holographic display.
Demonstration of simultaneous amplitude and phase modulation using complex-amplitude Fresnel holography.

Movie S5. Comparison of holographic display reconstructed from POH and CAH.
Dynamic comparison of holographic reconstructions from POH and CAH designs using an archery video.

Movie S6. Dual display of an amplitude profile and a Fresnel holographic image.
Simultaneous presentation of a grayscale amplitude image at the PDM plane and a reconstructed Fresnel hologram at the object plane.

Movie S7. Point-element-based holographic display.
Demonstration of dynamic holographic reconstruction using point-element-based encoding.

Movie S8. 3D spiral focusing.
Demonstration of dynamic multi-focus optical field generation along a 3D spiral trajectory.

Movie S9. 2D Patterned beam steering.
Dynamic scanning demonstration of a "HUST" logo using patterned beam steering, highlighting high-speed modulation capability.

Reference

1. Yu, N. *et al.* Light propagation with phase discontinuities: generalized laws of reflection and refraction. *Science* **334**, 333–337 (2011).

2. Sun, S. *et al.* Gradient-index meta-surfaces as a bridge linking propagating waves and surface waves. *Nat. Mater.* **11**, 426–431 (2012).

3. Balthasar Mueller, J. P., Rubin, N. A., Devlin, R. C., Groever, B. & Capasso, F. Metasurface Polarization Optics: Independent Phase Control of Arbitrary Orthogonal States of Polarization. *Phys. Rev. Lett.* **118**, 113901 (2017).

4. Huard, S. *Polarization of Light*. (John Wiley ; Masson, Chichester ; New York : Paris, 1997).

5. Xie, Q., Yu, S.-T., Wang, X.-K., Zheng, Y.-G. & Yuan, Z.-S. DMD-based pure-phase superpixel method for digital holography. *Appl. Phys. Express* **16**, 012009 (2023).

6. Goorden, S. A., Bertolotti, J. & Mosk, A. P. Superpixel-based spatial amplitude and phase modulation using a digital micromirror device. *Opt. Express* **22**, 17999 (2014).

7. Saha, S. K. *et al.* Scalable submicrometer additive manufacturing. *Science* **366**, 105–109 (2019).

8. Park, J. *et al.* All-solid-state spatial light modulator with independent phase and amplitude control for three-dimensional LiDAR applications. *Nat. Nanotechnol.* **16**, 69–76 (2021).

9. HOLOEYE LC2012 spatial light modulator. https://holoeye.com/products/spatial-light-modulators/lc-2012-spatial-light-modulator-transmissive/.

10. Meadowlark Optics 1024 x 1024 spatial light modulator. *Meadowlark Optics* https://www.meadowlark.com/shop/slms/1024-x-1024-spatial-light-modulator/.

11. Hamamatsu LCOS-SLM. https://www.hamamatsu.com/us/en/product/optical-components/lcos-slm.html.

12. Meadowlark Optics 1920 x 1200 spatial light modulator. *Meadowlark Optics* https://www.meadowlark.com/shop/slms/1920-x-1200-spatial-light-modulator/.

13. Texas Instruments DLP471TE data sheet. https://www.ti.com/product/DLP471TE.

14. HOLOEYE GAEA-2.1 phase only LCOS-SLM. https://holoeye.com/products/spatial-light-modulators/gaea-2-phase-only/.

15. Amari, K. *et al.* Novel CMOS-backplane technologies for fine pixel pitch and high image quality of LCOS microdisplay. *Proc. Int. Disp. Workshop* 173 (2021) doi:10.36463/idw.2021.0173.

16. Huang, Y.-W. *et al.* Gate-Tunable Conducting Oxide Metasurfaces. *Nano Lett.* **16**, 5319–5325 (2016).

17. Shirmanesh, G. K., Sokhoyan, R., Wu, P. C. & Atwater, H. A. Electro-optically Tunable Multifunctional Metasurfaces. *ACS Nano* **14**, 6912–6920 (2020).

18. Sisler, J. *et al.* Electrically tunable space–time metasurfaces at optical frequencies. *Nat. Nanotechnol.* **19**, 1491–1498 (2024).

19. Fang, Z. *et al.* Nonvolatile phase-only transmissive spatial light modulator with electrical addressability of individual pixels. *ACS Nano* **18**, 11245–11256 (2024).

20. Benea-Chelmus, I.-C. *et al.* Electro-optic spatial light modulator from an engineered organic layer. *Nat. Commun.* **12**, 5928 (2021).

21. Li, S.-Q. *et al.* Phase-only transmissive spatial light modulator based on tunable dielectric metasurface. *Science* **364**, 1087–1090 (2019).

22. Mansha, S. *et al.* High resolution multispectral spatial light modulators based on tunable Fabry-Perot nanocavities. *Light Sci. Appl.* **11**, 141 (2022).

23. Moitra, P. *et al.* Electrically tunable reflective metasurfaces with continuous and full-phase modulation for high-efficiency wavefront control at visible frequencies. *ACS Nano* **17**, 16952–16959 (2023).

24. Kuznetsov, A. I. Flat optics and nanoantenna spatial light modulators for imaging, LiDAR, and 3D holographic display applications. in *High Contrast Metastructures XIII* (eds. Chang-Hasnain, C. J., Zhou, W. & Alù, A.) 20 (SPIE, San Francisco, United States, 2024). doi:10.1117/12.2692860.